

Skin-Friction and Forced Convection from Rough and Smooth Plates

Aubrey G. Jaffer
e-mail: agj@alum.mit.edu

Abstract

Since the 1930s, theories of skin-friction drag from plates with rough surfaces have been based on an analogy to turbulent flow within pipes having rough interiors. Failure of this analogy at low Reynolds number (Re) flow rates has frustrated attempts to create a comprehensive theory.

By introducing the concept of self-similar roughness, this investigation derives formulas for a plate's skin-friction drag coefficient and forced convection given its root-mean-squared (RMS) height-of-roughness and isotropic spatial period. These formulas match measurements from Pimenta, Moffat, and Kays (1975), Bergstrom, Akinlade, and Tachie (2005), and experiments conducted for this investigation within their expected measurement uncertainties.

Building on its analysis of self-similar roughness, this investigation also derives a formula for the skin-friction coefficient of a smooth plate; this formula matches measurements from Smith and Walker (1959) and Spalding and Chi (1964) spanning four orders of magnitude of Re with 0.75% RMS relative error. Its new formula for smooth turbulent forced convection is in agreement with Lienhard (2020), while expanding the range to all fluid Prandtl numbers.

This research did not receive any specific grant from funding agencies in the public, commercial, or not-for-profit sectors.

Table of contents

1. <i>Introduction</i>	2
2. <i>Roughness metrics</i>	4
3. <i>Formulas from prior works</i>	6
4. <i>Rough turbulence</i>	7
5. <i>Profile roughness</i>	7
6. <i>Self-similar ramp permutations</i>	8
7. <i>Friction travel and velocity</i>	9
8. <i>Skin-friction from a rough plate</i>	10
9. <i>Skin-friction from a smooth plate</i>	10
10. <i>Spectral roughness</i>	12
11. <i>Periodic roughness</i>	13
12. <i>Onset of rough turbulence</i>	14
13. <i>Flat-peaked roughness</i>	15
14. <i>Local skin-friction</i>	17
15. <i>Forced convection from a rough plate</i>	18
16. <i>Forced convection from a smooth plate</i>	18
17. <i>Periodic smoothness and laminar flow</i>	22
18. <i>Turbulent flow modes</i>	23
19. <i>Fully rough regime</i>	24
20. <i>Smooth plate and sandpaper</i>	26
21. <i>Woven wire mesh</i>	27
22. <i>Perforated sheet</i>	28
23. <i>Forced convection measurements</i>	29
24. <i>Cloth tape</i>	30
25. <i>Discussion</i>	31
26. <i>Conclusions</i>	32
27. <i>Nomenclature</i>	33
28. <i>References</i>	34
29. <i>Appendix: convection measurement apparatus and methodology</i>	35

1. Introduction

Drag is the pressure opposing fluid flow by an object. Drag consists of “form drag”, due to fluid being deflected around the object, and “skin-friction drag” (or “resistance”) due to dissipation of the viscous friction stress (shearing stress) generated by flow along the object’s surface. A related phenomenon, “forced convection”, is the heat transfer to or from a surface induced by flow along that surface. Skin-friction and forced convection are relevant to a wide range of scientific and engineering disciplines.

Circa 1930, Prandtl [1] and von Kármán [2] developed theories for frictional resistance along (smooth) plates from the results of research on flow through pipes; this is the “pipe-plate analogy”.

In 1934, Prandtl and Schlichting [3] developed a theory of skin-friction resistance for rough plates based on their analysis of Nikuradse’s [4] measurements of sand glued inside pipes (“sand-roughness”). The conclusion of the (translated) paper states:

“The resistance law just derived for rough plates has chiefly validity for a very specific type of roughness, namely a smooth surface to which sand grains have been densely attached and where the Nikuradse pipe results have been taken as the basis. . .

A single roughness parameter (the relative roughness) will in all likelihood no longer answer the purpose in continued investigations of the roughness problem.”

In 1936, Schlichting [5] investigated the velocity field and skin-friction of water flowing through a closed rectangular channel having one wall replaced in turn by a series of plates, each having an array of identical protrusions attached: spheres, spherical caps (bumps), or cones. The protrusions were positioned on the plates in a hexagonal array which was elongated 15% in the direction of flow.

There was significant pressure drop between the inflow and outflow of the channel, so it was not a case of the isobaric (no pressure drop) flow which occurs along external plates. The similarity of closed channel flow to pipe flow is well known, but does not support or refute treating rough pipe interiors and plates analogously.

In 1954, Hama [6] described three challenges to the pipe-plate analogy:

“Now there is no obvious reason why pipe flow and boundary-layer flow should be identical or even similar. First, a pressure gradient is essential for flow through a pipe but not along a plate. Second, pipe flow is confined and perforce uniform, while flow along a plate develops semi-freely and bears no such a priori guarantee of displaying similar velocity profiles at successive sections. Finally, the diameter and roughness size are the only geometrical dimensions of established flow in pipes, whereas at least three linear quantities are necessary to characterize the boundary-layer.”

Fluid in contact with the plate surface has zero velocity. The “boundary-layer” is flow near the surface which has velocity different from the bulk flow (or “free-stream”) velocity u .

Hama attempted to confirm the pipe-plate analogy with measurements of wire screens affixed to smooth plates, but concluded that it was confirmed only in the fully rough regime (defined below).

Roughness in prior works [3, 4, 5, 6, 7, 8, 9, 10, 11] is reported as sand-roughness k_S , the height of “coarse and tightly placed roughness elements such as, for example, coarse sand grains glued on the surface” [9].

Testing a machined analogue to sand-roughness, Pimenta, Moffat, and Kays [7] wrote in 1975 that, while the agreement of their data with the Prandtl-Schlichting plate model was “rather good” in the fully rough regime, their apparatus did not have the same behavior as “Nikuradse’s sand-grain pipe flows in the transition region.”

By modeling the wake component of the velocity profile, in 1985 Mills and Hang [8] presented a formula improving the match to Pimenta et al data in the rough regime, but was silent about other flow regimes.

Along with laminar flow, the theory for flow within pipes (and channels) distinguishes three turbulent flow regimes: smooth, (fully) rough, and transitional. Smooth turbulent pipe flow encounters viscous resistance which varies inversely with the ratio of fluid velocity to viscosity. Rough pipe flow encounters resistance which varies with the height-of-roughness, while the effect of viscosity is negligible. The transitional regime describes the range of flow rates where both viscosity and roughness affect the resistance (Colebrook [12]).

The Reynolds number (Re) is used to represent the bulk fluid flow rate (far from the plate); Reynolds numbers with subscripts are used to represent other flow rates. The local Reynolds number $Re_x = x Re/L$, where x is the distance from the leading edge of the plate in the direction of flow, and characteristic-length L is the length scale for the physical system. Except where stated otherwise in this investigation, L is plate length in the direction of flow.

Drag in prior works is represented by the local drag coefficient c_f or C_f , which is a function of x/k_S , and of the Reynolds number or a subscripted Reynolds number.

Prandtl and Schlichting [3] specified the boundaries between flow regimes using the “sand-roughness Reynolds number” Re_k . For plates, they assigned the boundaries between smooth, transitional, and rough regimes at $Re_k = 7.08$ and 70.8 . Pimenta et al [7] gave $Re_k = 65$ as the transitional-to-rough boundary.

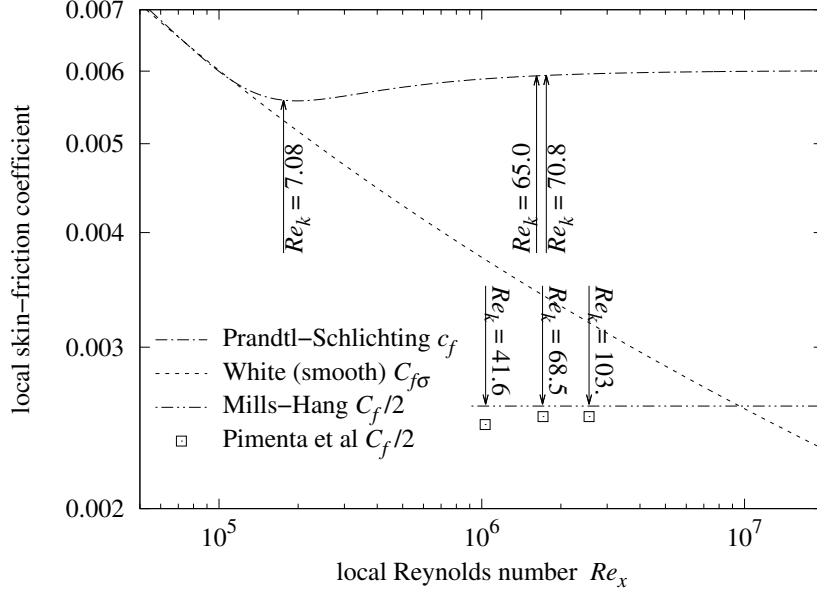


Figure 1 local c_f versus Re_x

Figure 1 presents skin-friction coefficient curves, Re_k regime boundaries and values, and measurements from a plate having relative sand-roughness $x/k_S = 1200$.

In pipes, the resistance of rough flow is never less than the resistance of smooth turbulent flow occurring in otherwise identical conditions. A tenet of the rough pipe-plate analogy is that this rule also applies to rough, external plates; for example, the “Prandtl-Schlichting c_f ” curve is never less than the “White (smooth) $C_{f\sigma}$ ” curve in Figure 1.

The Pimenta et al measurements are much closer to $c_f/2$ than they are to c_f . Moreover, while Pimenta et al and Mills-Hang both named their skin-friction coefficients $C_f/2$, it does not change the fact that all three measurements are less than the smooth turbulent coefficient $C_{f\sigma}$. Thus, these measurements can not be in any turbulent flow regime; the remaining alternative is laminar flow. Laminar flow coefficients have a steeper slope than $C_{f\sigma}$; yet these measurements are nearly at the constant level predicted by Mills and Hang $C_f/2$ for the rough regime.

This is where the pipe-plate analogy fails for roughness. Rough turbulent skin-friction coefficients can have values less than smooth turbulent coefficients for external plates, but not inside pipes.

Nevertheless, research continued based on the pipe-plate analogy. A 2004 survey article by Jiménez [13] expressed enduring faith in the rough pipe-plate analogy: “The theoretical arguments are sound, but the experimental evidence is inconclusive.”

In 2001 Tachie, Bergstrom, Balachandar, and Ramachandran [14] combined multiple studies to propose a correlation for skin-friction coefficient in terms of the momentum-thickness Reynolds number Re_θ :

$$C_f = [4.13 \times 10^{-2} - 2.68 \times 10^{-2} \log_{10} Re_\theta + 6.528 \times 10^{-3} \log_{10}^2 Re_\theta - 5.54 \times 10^{-4} \log_{10}^3 Re_\theta] \pm 7\% \quad 150 < Re_\theta < 15000 \quad (1)$$

In terms of a roughness metric, formula (1) has no predictive value because Re_θ must be computed from velocity field measurements along the surface in question.

Bergstrom, Akinlade, and Tachie [15], performed experiments with sandpapers, woven-wire meshes, and perforated sheets attached to flat plates in 2005. They found that the local skin-friction coefficient c_f satisfied:

$$c_f^{1/2} = [0.360 \pm 0.025] \frac{\delta^*}{\delta} \quad (2)$$

where δ^* is the displacement thickness and δ is the (99% velocity) boundary-layer thickness. In terms of a roughness metric, formula (2) also has no predictive value because both δ^* and δ must be computed from velocity field measurements along the surface in question. Fortunately, they included free-stream velocity in their tables, allowing their skin-friction measurements to be compared with the present theory.

Lastly, an additional complication was described by S. F. Hoerner in the discussion appended to Hama [6]:

“One conclusion from sand experiments has been the expectation that from then on every rough surface should have a constant terminal drag coefficient. As early as 1924, it has been demonstrated (by Hopf and Fromm in *Zeitschr. Angew. Math. Mech.*, 1923:329-339) that certain types of roughness do not show any constant coefficients.”

The sand-roughness metric’s lack of generality, the need for additional roughness parameters, non-constant terminal drag coefficients, and the failure of the pipe-plate analogy for roughness motivate and justify a fresh theoretical analysis of isobaric flow along plate roughness which is based on a traceable roughness metric.

2. Roughness metrics

Two established, traceable roughness metrics are the root-mean-squared (RMS) height-of-roughness and the arithmetic-mean height-of-roughness. For an elevation function $z(x, y)$ defined on area A having a convex perimeter, its mean elevation \bar{z} and RMS height-of-roughness ε are:

$$\bar{z} = \int_A z \, dA / \int_A dA \quad \varepsilon = \sqrt{\int_A |z - \bar{z}|^2 \, dA / \int_A dA} \quad (3)$$

The arithmetic-mean height-of-roughness is defined in terms of the same mean elevation \bar{z} :

$$\int_A |z - \bar{z}| \, dA / \int_A dA \quad (4)$$

Modeling sand-roughness grains as diameter k_S spheres sitting in a sea of depth g glue, the mean elevation \bar{z} of a cell of area A containing one sphere is:

$$\bar{z} = \int_0^{k_S/2} \frac{2\pi x}{A} \left[\sqrt{\frac{k_S^2}{4} - x^2} + \frac{k_S}{2} \right] dx + \left[A - \frac{\pi k_S^2}{4} \right] \frac{g}{A} = g + \frac{5\pi k_S^3}{24A} - \frac{\pi k_S^2 g}{4A} \quad (5)$$

From formula (3), its RMS height-of-roughness ε is:

$$\varepsilon(k_S, g, A) = \sqrt{\int_0^{k_S/2} \frac{2\pi x}{A} \left| \sqrt{\frac{k_S^2}{4} - x^2} + \frac{k_S}{2} - \bar{z} \right|^2 dx + \left[1 - \frac{\pi k_S^2}{4A} \right] |g - \bar{z}|^2} \quad (6)$$

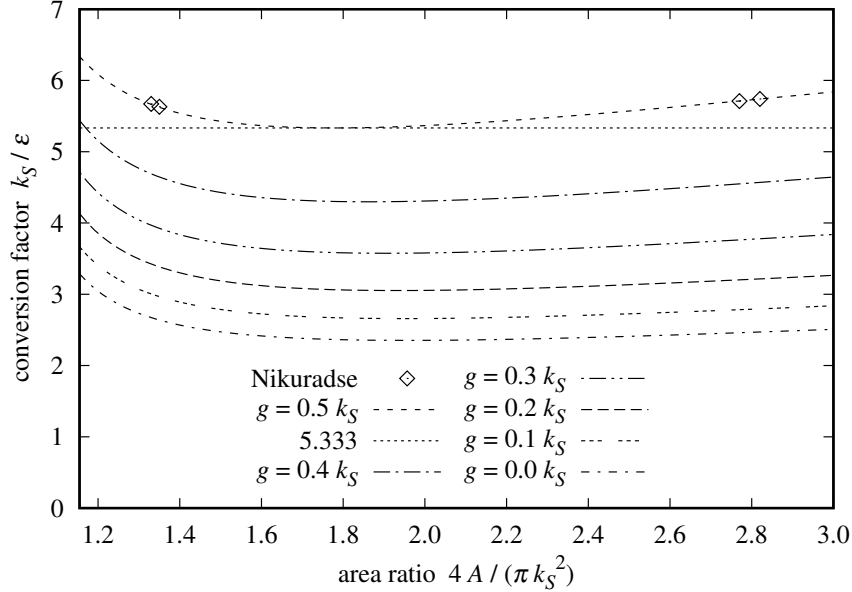


Figure 2 k_S/ε versus cell area of sand-roughness

Figure 2 shows k_S/ε versus the cell/shadow area ratio, at six glue-levels from 0% to 50% of k_S . Table 1 lists k_S , grain densities, and conversion factors for Nikuradse’s [4] sand coatings, assuming $g = 0.5 k_S$.

k_S	grains/cm ²	k_S/ε @ $g = 0.5 k_S$
.08 cm	150	5.67
.04 cm	590	5.63
.02 cm	1130	5.74
.01 cm	4600	5.71

Table 1 Nikuradse’s sand coatings

Afzal, Seena, and Bushra [16] fit 5.333 for the RMS to sand-roughness conversion factor k_S/ε , and 6.45 for the arithmetic-mean to sand-roughness ratio in pipes. $k_S/\varepsilon = 5.333$ is a broad minimum for the $g/k_S = 0.5$ curve in Figure 2.

The “ k_S/ε @ $g = 0.5 k_S$ ” column values in Table 1 (“Nikuradse” in Figure 2) match each other within 2%. The tightest spread on Table 1 data with the arithmetic-mean height-of-roughness exceeds 20%. Thus, sand-roughness correlates an order of magnitude more strongly with the RMS height-of-roughness than with the arithmetic-mean.

Flack, Schultz, Barros, and Kim [17] measured skin-friction from grit-blasted surfaces in a duct. They wrote “The root-mean-square roughness height is shown to be most strongly correlated with the equivalent sand-roughness height (k_S) for the grit-blasted surfaces.”

The plate tested by Pimenta et al [7] was composed of 11 layers of densely packed 1.27 mm diameter metal spheres “arranged such that the surface has a regular array of hemispherical roughness elements.” There was no sea of glue surrounding the spheres. Shrinking the cell to the sphere’s shadow, $\pi k_S^2/4$, the RMS height-of-roughness of the top half of the 1.27 mm sphere is 0.150 mm. Converting $k_S = 0.794$ mm from Pimenta et al by the 5.333 conversion factor from Afzal et al [16] yields $k_S/5.333 \approx 0.149$ mm, which matches 0.150 mm within 1%.

3. Formulas from prior works

In *Boundary-layer theory* [9], Prandtl and Schlichting give formulas for fully rough local (c_f) and plate average ($\overline{c_f}$) skin-friction coefficient for a rough plate in terms of x/k_S and L/k_S , respectively.

$$c_f = \left[2.87 + 1.58 \log_{10} \frac{x}{k_S} \right]^{-2.5} \quad x \leq L \quad (7)$$

$$\overline{c_f} = \left[1.89 + 1.62 \log_{10} \frac{L}{k_S} \right]^{-2.5} \quad 10^2 < \frac{L}{k_S} < 10^6 \quad (8)$$

Mills and Hang [8] give a formula (9) which is more accurate than formula (7) on the local skin-friction measurements from Pimenta et al [7]. Their local (C_f) and average ($\overline{C_f}$) coefficient formulas are:

$$C_f = \left[3.476 + 0.707 \ln \frac{x}{k_S} \right]^{-2.46} \quad 750 < \frac{x}{k_S} < 2750 \quad (9)$$

$$\overline{C_f} = \left[2.635 + 0.618 \ln \frac{L}{k_S} \right]^{-2.57} \quad (10)$$

White [10] gives formula (11) for fully rough local skin-friction coefficient:

$$C_f = \left[1.4 + 3.7 \log_{10} \frac{x}{k_S} \right]^{-2} \quad \frac{x}{k_S} > \frac{Re_x}{1000} \quad (11)$$

White is also the source of a widely used formula for turbulent skin-friction coefficient for smooth plates:

$$C_{f\sigma}(Re_x) = \frac{0.455}{\ln^2(0.06 Re_x)} \quad (12)$$

Mills and Hang [8] derived the average formula (10) from the local formula (9) by fitting a curve to the result of the numerical integration in formula (13):

$$\overline{C_f} \left(\frac{L}{k_S} \right) = \frac{k_S}{L - L_0} \int_{L_0/k_S}^{L/k_S} C_f(x) dx \quad (13)$$

The local formulas (7), (9), and (11) each have a singularity where the expression containing the logarithm is zero. The lower limit of integration (L_0/k_S) must be large enough to avoid this; but the lower limit is not revealed in the prior works. The averaging formula (13) is quite sensitive to the lower limit because the largest value of the local formula occurs there.

For the Mills-Hang formula (9), with lower bound $L_0/k_S = 1.6$ and initial $dx/k_S = 0.01$, integration of the local C_f is within $\pm 0.5\%$ of the average $\overline{C_f}$ in formula (10) over the range $200 < x/k_S < 200 \times 10^3$.

For the Prandtl-Schlichting formula (7), with lower bound $L_0/k_S = 0.5$ and initial $dx/k_S = 0.5$, integration of the local c_f is within $\pm 0.5\%$ of the average $\overline{c_f}$ in formula (8) over the range $200 < x/k_S < 200 \times 10^3$.

Churchill [11] compared 8 formulas from various sources with the data from Pimenta et al [7]; it did not find any to be significantly closer than the Mills-Hang local formula (9).

Churchill had distinct formulas for computing the average (mean) skin-friction C_m from local C_f for smooth and rough surfaces, respectively:

$$C_m = C_f \frac{1 - 4.516\sqrt{C_f}}{1 - 7.965\sqrt{C_f} + 21.52 C_f} \quad C_m = C_f \frac{1 - 4.516\sqrt{C_f}}{1 - 7.965\sqrt{C_f}} \quad (14)$$

4. Rough turbulence

Forced flow along a plate with a rough surface is different in character from forced flow along a smooth surface because roughness disrupts what would otherwise be a viscous sub-layer adjacent to the plate. Lienhard and Lienhard [18] teaches: “Even a small wall roughness can disrupt this thin sublayer, causing a large decrease in the thermal resistance (but also a large increase in the wall shear stress).”

Jiménez [13] wrote “In flows with $\delta/k < 50$, the effect of the roughness extends across the boundary-layer, and is also variable. There is little left of the original wall-flow dynamics in these flows, which can perhaps be better described as flows over obstacles.”

This investigation focuses initially on the case where flow over obstacles dominates the dynamics. It does this by modeling the rough shearing stress as resulting from the interaction of flow with a roughness which disrupts flow at a succession of scales from L converging to 0. While simpler surfaces may also produce rough turbulence, a roughness which disrupts at this succession of scales surely will. Self-similarity can be used to succinctly describe such roughness across scales.

The turbulent boundary-layer thickness along a smooth plate increases proportionally to $x^{4/5}$, where x is the distance from its leading edge (Schlichting [9]). Roughness whose envelope height increases linearly with x can disrupt emerging boundary-layers repeatedly along the entire plate.

This approach departs from prior works which (in accord with the pipe-plate analogy) related the characteristic-length to the rough turbulent boundary-layer thickness. Roughness-as-disruption is incompatible with a continuous boundary-layer. Hence, except where stated otherwise in this investigation, the characteristic-length L is the length of the plate in the direction of flow.

5. Profile roughness

Simpler than surface roughness, roughness profiles can nonetheless be informative.

Let “profile roughness” be a function $z(x)$ with $0 \leq x \leq L$. Given a roughness profile $z(x)$, its mean elevation \bar{z} and RMS height-of-roughness ϵ (note the symbol difference from surface roughness ε) are:

$$\bar{z} = \frac{1}{L} \int_0^L z(x) dx \quad \epsilon = \sqrt{\frac{1}{L} \int_0^L |z(x) - \bar{z}|^2 dx} \quad (15)$$

Let “self-similar profile roughness” be a profile roughness function $z(x)$ with (integer) branching factor $n \geq 2$ such that the RMS height-of-roughness of $z(x)$ over an interval $x_0 < x < x_n$ is n times the RMS height-of-roughness of $z(x)$ over each equally divided sub-interval $x_t < x < x_{t+1}$ for $0 \leq t < n$ at a succession of scales converging to zero. Note that each $z(x_t)$ value contributes to its parent interval height-of-roughness, but not to any sub-interval.

A consequence of this definition is that the ratio of the length of an interval to the RMS height-of-roughness of z over that interval will be invariant over its succession of scales.

Of particular interest are self-similar roughness profiles which are permutations of the linear ramp $z(x) = \varsigma x/L$ with $0 \leq x \leq L$. Every elevation from 0 to peak height ς occurs exactly once in a ramp-permutation. The only occurrence of x in formula (15) is $z(x)$; hence the RMS height-of-roughness calculation depends only on the z values, not on their relation to x . Thus, the height-of-roughness of any ramp-permutation is identical to the height-of-roughness of the linear ramp:

$$\epsilon = \sqrt{\frac{1}{L} \int_0^L \left[\frac{\varsigma x}{L} - \frac{\varsigma}{2} \right]^2 dx} = \frac{\varsigma}{\sqrt{12}} \quad (16)$$

6. Self-similar ramp permutations

A self-similar integer sequence $Y(t, w)$ from integers $0 \leq t < w = n^q$ allows self-similar behavior to be explored with a finite approximation. Letting $t = \lfloor wx/L \rfloor \equiv \text{floor}(wx/L)$ constructs a roughness profile from a sequence by $z(x) = (\varsigma/w)Y(\lfloor wx/L \rfloor, w)$. These three examples are $n = 2$ ramp-permutation sequences:

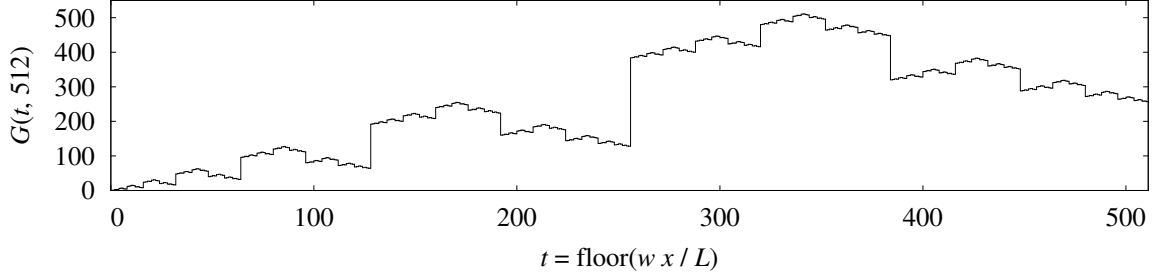


Figure 3 Gray-code profile roughness

Self-similar recurrence (17) defines the integer Gray-code sequence $G(t, w)$ shown in Figure 3.

$$G(t, w) = \begin{cases} t, & \text{if } w = 1; \\ w + G(w - 1 - (t \bmod w), w/2), & \text{if } \lfloor t/w \rfloor = 1; \\ G(t \bmod w, w/2), & \text{otherwise.} \end{cases} \quad (17)$$

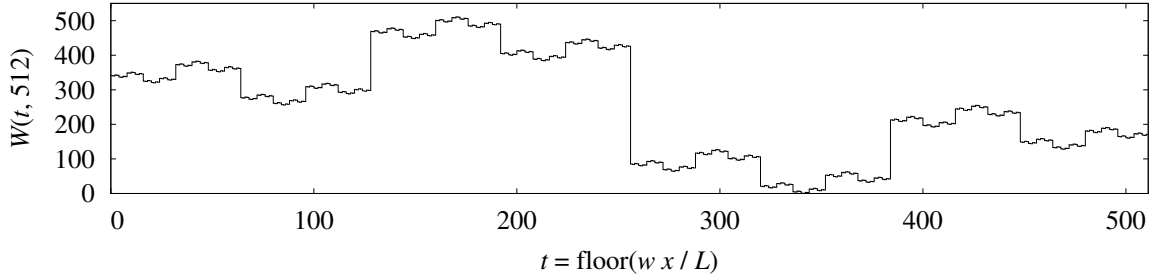


Figure 4 wiggliest self-similar profile roughness

Recurrence (18) defines the integer sequence $W(t, w)$ shown in Figure 4; it reverses direction at each bifurcation, yielding a wiggliest possible self-similar ramp-permutation sequence.

$$W(t, w) = \begin{cases} t, & \text{if } w = 1; \\ \lfloor t/w \rfloor w + W(w - 1 - (t \bmod w), w/2), & \text{otherwise.} \end{cases} \quad (18)$$

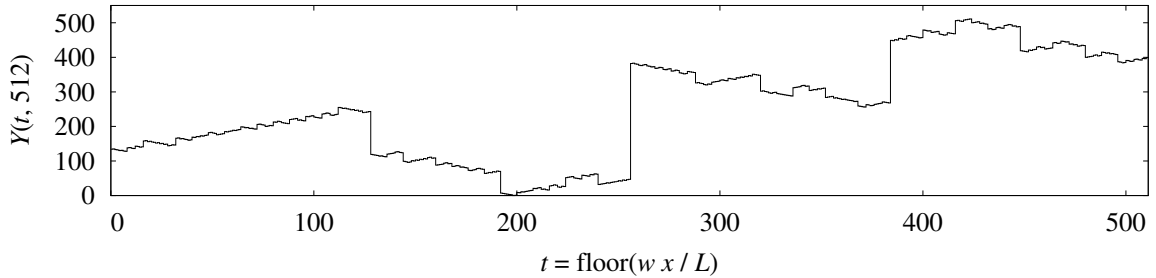


Figure 5 random reversal bifurcation profile roughness

Figure 5 shows a sequence generated by randomly reversing or not at each bifurcation in recurrence (19).

$$Y(t, w) = \begin{cases} t, & \text{if } w = 1; \\ w + Y(w - 1 - (t \bmod w), w/2), & \text{with probability 0.5;} \\ Y(t \bmod w, w/2), & \text{otherwise.} \end{cases} \quad (19)$$

For a given $w = 2^q \geq 4$, there are $2^w = 2^{[2^q]}$ distinct self-similar ramp-permutation sequences, but only 2 distinct ramp and 2 distinct wiggliest sequences.

7. Friction travel and velocity

In the conversion of bulk flow to rough turbulence, some particles of fluid must move in directions not parallel to the bulk flow. Such movement can result from the deflections of flow by roughness peaks, ridges, and valleys; the amount of turbulence induced by a roughness should grow as its height-of-roughness increases.

Let “run” be the horizontal axis and “friction” be the vertical axis of a profile roughness such as in Figure 5. For an integer ramp-permutation sequence $Y(t, w)$, the sum of the (dimensionless) lengths of all run segments is $w - 1 = 2^q - 1$. The sum of the friction segment lengths is:

$$\sum_{t=0}^{2^q-2} |Y(t, 2^q) - Y(t+1, 2^q)| \quad (20)$$

If a particle of fluid were to trace the ramp-permutation sequence $Y(t, w)$ from $t = 0$ to $t = w - 1$, then $w - 1$ is the run distance it would travel, while formula (20) is the friction distance.

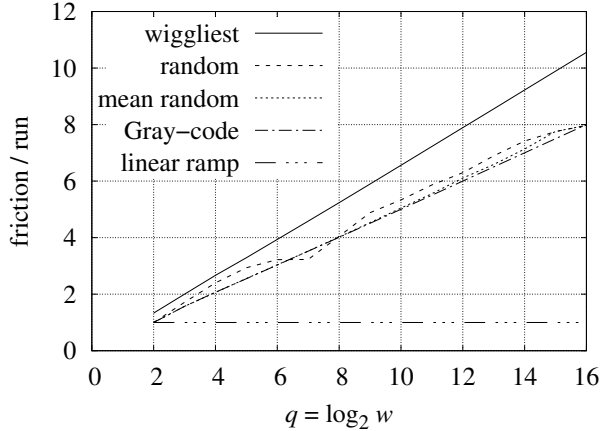


Figure 6 travel along profile roughness

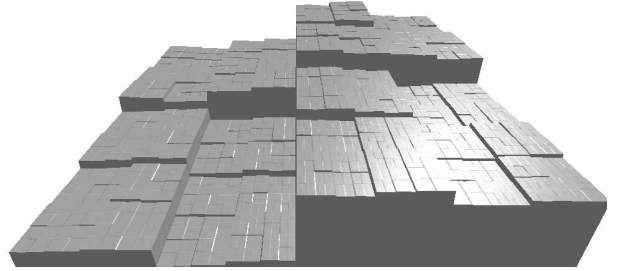


Figure 7 random reversal ramp surface

Figure 6 shows the friction travel to run travel ratio versus q , the base-2 logarithm of w . The slope is 0 for the linear ramp, $1/2$ for the Gray-code, approximately $1/2$ for the random reversal cases, and $2/3$ for the wiggliest roughness.

A wiggliest roughness sequence $W(t, w)$ is an extreme case; it reverses friction direction at each increment of run (t). For each wiggliest roughness sequence with $w \geq 4$ there are $2^{w-1} - 2$ other random reversal roughness sequences. The linear ramp never reverses direction. For each linear ramp sequence there are $2^{w-1} - 2$ other random reversal sequences. Being outliers, $W(t, w)$ and linear ramps are excluded from further consideration as roughness.

In Figure 6, the friction to run ratios for Gray-code and random reversal sequences are close to:

$$\frac{q}{2} \equiv \frac{\log_2 w}{2} \quad (21)$$

$Y(t, w)$, t , and w are dimensionless. The friction to run ratio (21) needs to be reformulated in terms of the height-of-roughness. Turning to dimensional analysis, the argument to \log_2 must be dimensionless, involve ϵ , and be greater than 1, so that the logarithm will be positive. This ratio must increase with increasing ϵ ; thus, ϵ and the logarithm will be in denominators, yielding a friction travel to run travel ratio:

$$\frac{2}{\log_2(L/\epsilon)} \quad (22)$$

Scaling formula (22) by $1/\sqrt{12}$ from formula (16) converts formula (22) into the ratio of RMS friction travel to run travel:

$$\frac{1}{\sqrt{12}} \frac{2}{\log_2(L/\epsilon)} = \frac{1}{\sqrt{3} \log_2(L/\epsilon)} \quad (23)$$

Considering the run travel and friction travel with respect to time lets formula (23) also serve as the ratio of friction velocity u_τ to bulk flow velocity u .

8. Skin-friction from a rough plate

Newberry and Savage [19] demonstrated that some self-similar systems which are modeled using continuous power-law probability distributions can be modeled using discrete power-law distributions.

This investigation uses that idea in reverse. The conversion of run velocity into friction velocity by contact with discrete self-similar $n = 2$ roughness was modeled by formula (23); the u_τ/u conversion ratio for a random self-similar roughness will be inferred using a random variable.

Instead of summing $|Y(t, 2^q) - Y(t + 1, 2^q)|$ as in formula (20), the analogous mean field theory is to integrate $Z > 0$, a continuous random variable having a Pareto distribution where the frequency of Z is inversely proportional to Z^2 :

$$1 / \left[\sqrt{3} \int_\epsilon^L \frac{Z}{Z^2} dZ \right] = \frac{1}{\sqrt{3} \ln(L/\epsilon)} \quad (24)$$

Although vortexes can arise in 2-dimensional systems, turbulence is a 3-dimensional phenomenon. A plate surface composed of parallel, edge-to-edge ridges and valleys will disrupt flow which is perpendicular to the ridges, but not disrupt flow which is parallel to the ridges. To avoid this complication, this investigation considers only surface roughness which is “isotropic”: rotating the flow azimuth in the plane of the rough surface does not substantially affect its behavior.

In the generalization of formula (23) to random self-similar roughness in formula (24), the profile height-of-roughness ϵ was replaced by the surface height-of-roughness ϵ . As with the profile RMS height-of-roughness, the surface RMS height-of-roughness of any permutation of the linear ramp from 0 to ς is $\varsigma/\sqrt{12}$. Thus, the $1/\sqrt{3}$ coefficient is the same for the ϵ and ϵ formulas.

An example of self-similar ramp-permutation surface roughness is shown in Figure 7.

The skin-friction coefficient $\overline{f_c}$ is the ratio of the shearing stress τ_2 to the fluid flow’s dynamic pressure (kinetic energy density) $\rho u^2/2$, where u is bulk flow velocity and ρ is fluid density:

$$\overline{f_c} = \frac{\tau_2}{\rho u^2/2} \quad (25)$$

Both τ_2 and $\rho u^2/2$ have units of pressure, $\text{kg}/(\text{m} \cdot \text{s}^2)$; hence $\overline{f_c}$ is dimensionless. Multiplication by formula (24) converts bulk flow velocity u to friction velocity u_τ , from which τ_2 is derived:

$$u_\tau = \frac{u}{\sqrt{3} \ln(L/\epsilon)} \quad \tau_2 = \frac{\rho u_\tau^2}{2} = \frac{\rho u^2}{6 \ln^2(L/\epsilon)} \quad \frac{L}{\epsilon} \gg 1 \quad (26)$$

Combining equations (25) and (26) yields the formula for the average skin-friction coefficient $\overline{f_c}$ of an isotropic self-similar rough surface:

$$\overline{f_c} = \frac{1}{3 \ln^2(L/\epsilon)} \quad \frac{L}{\epsilon} \gg 1 \quad (27)$$

Prandtl and Schlichting [3] calculated $\tau = \rho u_\tau^2$, not $\tau_2 = \rho u_\tau^2/2$. As a result, the Prandtl-Schlichting $\overline{c_f}$ is (more than) twice the $\overline{f_c}$ of formula (27). Both Pimenta et al [7] and Mills and Hang [8] treat $c_f/2$ as the skin-friction coefficient.

Equation (27) is compared with measurements in Sections 19, 21, and 22.

9. Skin-friction from a smooth plate

For a given $Re \gg 1$ there must be a ratio L/ϵ so large that a plate of length L with self-similar roughness ϵ has turbulence-inducing behavior midway between that of a rough surface and that of a smooth surface.

Let the “roughness Reynolds number” Re_ϵ derive from friction velocity u_τ at scale ϵ :

$$Re_\epsilon = \frac{u_\tau \epsilon}{\nu} = \frac{u}{\sqrt{3} \ln(L/\epsilon)} \frac{\epsilon}{\nu} = \frac{Re}{\sqrt{3} [L/\epsilon] \ln(L/\epsilon)} \quad (28)$$

where ν is the fluid kinematic viscosity and $Re = Lu/\nu$. The Re strength at which rough plate skin-friction transitions to smooth plate skin-friction will have the same Re_ϵ value at all $L/\epsilon \gg 1$. Combining $Re_\epsilon = 1$ with formula (28) relates Re to L/ϵ at this transition:

$$Re = \sqrt{3} \frac{L}{\epsilon} \ln \frac{L}{\epsilon} \quad (29)$$

Relation (29) between Re and L/ε suggests that the smooth turbulent skin-friction coefficient can be inferred from formulas (27) and (29). However, there being no roughness on a smooth plate, $\overline{f_c}$ formula (27) must be adapted for this application. Scaling the L/ε argument to $\overline{f_c}$ by $1/e$ and $\overline{f_c}$ by $\sqrt[3]{2}$:

$$\overline{f_{c\sigma}} = \sqrt[3]{2} \overline{f_c} \left(\frac{L}{e\varepsilon} \right) = \sqrt[3]{2} \left[\frac{1}{3} \ln^{-2} \frac{L}{e\varepsilon} \right] \quad (30)$$

L/ε can be eliminated from formulas (29, 30) using the Lambert W function, which is the inverse of $\varphi \exp(\varphi)$. The inverse of $\vartheta = \varphi \ln(\varphi)$ is $\varphi = \exp(W_0(\vartheta))$, where W_0 is the principal branch of W.

$$\overline{f_{c\sigma}} = \frac{\sqrt[3]{2}}{3} \ln^{-2} \left(\frac{\exp(W_0(Re/\sqrt{3}))}{e} \right) = \frac{\sqrt[3]{2}/3}{[W_0(Re/\sqrt{3}) - 1]^2} \quad Re \gg \sqrt{3}e \quad (31)$$

Euler's number $e = \exp(1)$ is a fixed point of $\varphi \ln(\varphi)$ and of its inverse, $\exp(W_0(\vartheta))$. The coefficient $\sqrt[3]{2}/3 \approx 0.4200$. $Re \gg \sqrt{3}e \approx 4.71$ implies that smooth turbulence will not occur at $Re < 90$.

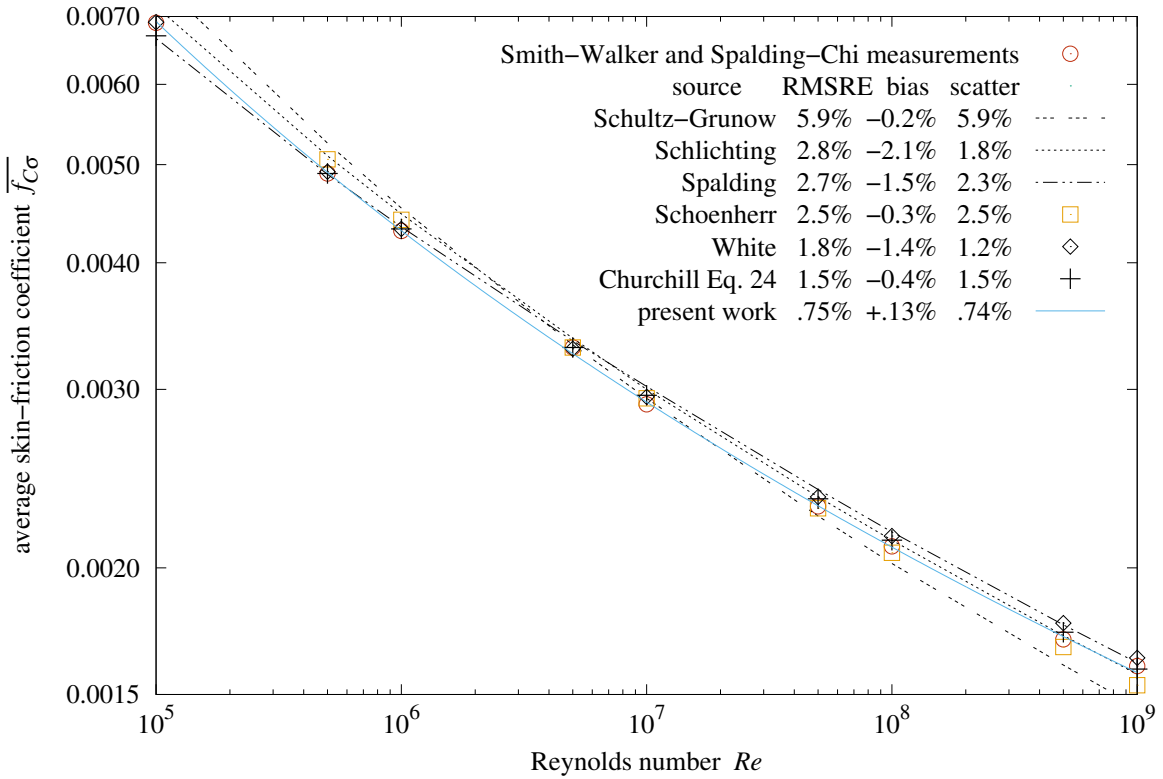


Figure 8 average $\overline{f_{c\sigma}}$ versus Re of smooth plate

Churchill [11] compared smooth turbulent skin-friction coefficient formulas from multiple sources with measurements from Smith and Walker [20], and Spalding and Chi [21]. Figure 8 plots average (not local) coefficient formulas from Churchill; the key gives the RMS error of the measurements relative to each formula.

RMS relative error (RMSRE) gauges the fit of measurements $g(Re)$ to a formula $f(Re)$, with each sample having equal weight. The RMS error of $g(Re)$ relative to $f(Re)$ at n points Re_j is:

$$\sqrt{\frac{1}{n} \sum_{j=1}^n \left| \frac{g(Re_j)}{f(Re_j)} - 1 \right|^2} \quad (32)$$

Figure 8's key splits RMSRE into bias and scatter. The root-sum-squared of bias and scatter is RMSRE.

The "Smith-Walker and Spalding-Chi measurements" have 0.75% RMSRE from the "present work" formula (31). This is significantly less error than any of the formulas evaluated by Churchill.

10. Spectral roughness

Several prior works [4, 5, 6, 8, 12] use the term “uniform roughness” to describe sand-roughness, implying that the height-of-roughness is the same at all scales. This concept of uniform roughness is incompatible with self-similarity; the RMS height-of-roughness of a portion of a self-similar surface must shrink with the succession of scales converging to 0.

Sand-roughness could be described as “repeated roughness”. However, a roughness having 1000 sand grains over its characteristic length L can also be described as having 500 sand grain pairs, and so on. An unambiguous method for determining the spatial period is needed.

The discrete Fourier transform converts a series of equally-spaced samples of a (roughness) function into complex coefficients for each of its harmonic sinusoidal components. There is a profound connection between the discrete Fourier transform X_j of a roughness sequence $Y(t, w)$ and its RMS height-of-roughness ϵ :

$$X_j = \sum_{t=0}^{w-1} Y(t, w) \exp\left(\frac{-2\pi i j t}{w}\right) \quad \epsilon = \sqrt{\frac{1}{w} \sum_{j=1}^{w-1} |X_j|^2} \quad (33)$$

Note that $|X_{w-j}| = |X_j|$ because all the $Y(t, w)$ elevations have imaginary parts = 0; hence there are $w/2 + 1$ distinct $|X_j|$; only $0 \leq j \leq w/2$ needs to be considered in the developments which follow.

Constant term $X_0 = \bar{z}$, the mean value of Y , is the only X_j term not included in the sum for ϵ . Because ϵ does not depend on X_0 , for $0 < j \leq w/2$, the X_j with the largest amplitude is the dominant component of roughness. Let the “period index” j_P be the index j of this X_j having the largest amplitude $|X_j|$.

When one $|X_j|$ is dominant, j_P is well-defined and the spatial period of the roughness is $L_P = L/j_P$.

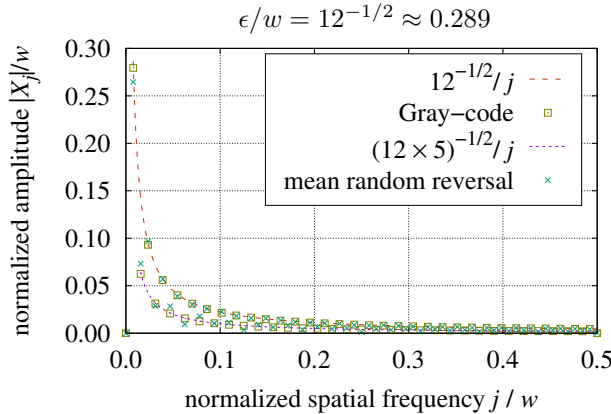


Figure 9 Gray and random spectra

Figure 9 shows the $|X_j|/w$ amplitude spectrum of the Gray-code roughness profile from Figure 3; also the mean Fourier spectrum amplitudes from 187 instances of 128-point random reversal profiles ($w = 128$). For both spectra, X_1 has the largest amplitude; thus $j_P = 1$, indicating that neither spectrum is from repeated roughness.

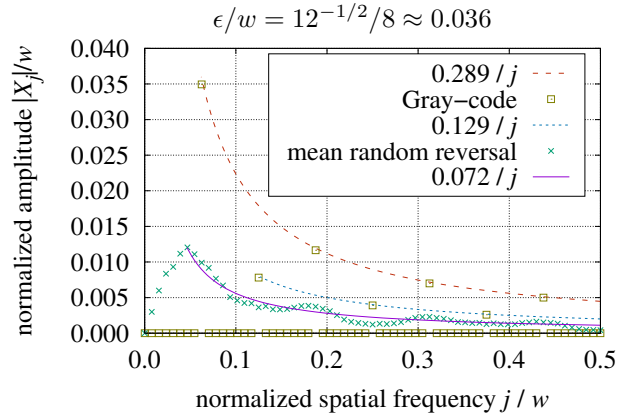


Figure 10 Gray and random eighths

Figure 10 shows the spectrum of eight concatenated repetitions of a Gray-code sequence, and the mean Fourier spectrum amplitudes from 187 instances of eight concatenated random reversal sequences. The period index j_P of the Gray-code eighths is 8, as expected; but the random reversal sequences have $j_P = 6$ because the amplitudes are not correlated between the random eighths.

Use of the discrete Fourier transform seems appropriate for detecting and quantifying the spatial period of profile roughness. The next section generalizes the spatial period metric to isotropic surface roughness.

11. Periodic roughness

Let “periodic roughness” be a surface composed of a regular array of many isotropic, uniformly sized patches, all sharing the same mean elevation \bar{z} and the same RMS height-of-roughness ε . Note that the mean elevation and RMS height-of-roughness for the surface as a whole will also be \bar{z} and ε , respectively.

Let $S_{s,t}$ be a $w \times w$ matrix of mean elevations from a $w \times w$ square tiling of an $L_w \times L_w$ region of a rough surface. Its 2-dimensional discrete spatial Fourier transform is:

$$X_{j,k} = \sum_{t=0}^{w-1} \sum_{s=0}^{w-1} S_{s,t} \exp\left(-2\pi i \frac{j t + k s}{w}\right) \quad (34)$$

Let the 2-dimensional period index $j_P = \sqrt{j^2 + k^2} > 0$, where $0 \leq j \leq w/2$ and $0 \leq k \leq w/2$ are the indexes of the coefficient $X_{j,k}$ having the largest amplitude. The 2-dimensional spatial period $L_P = L_w/j_P$.

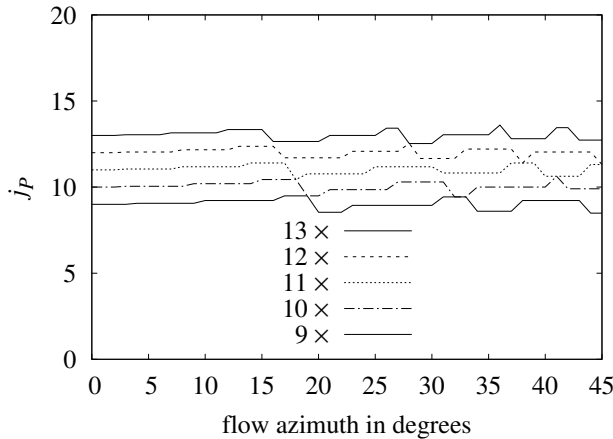


Figure 11 bi-level plate 50%

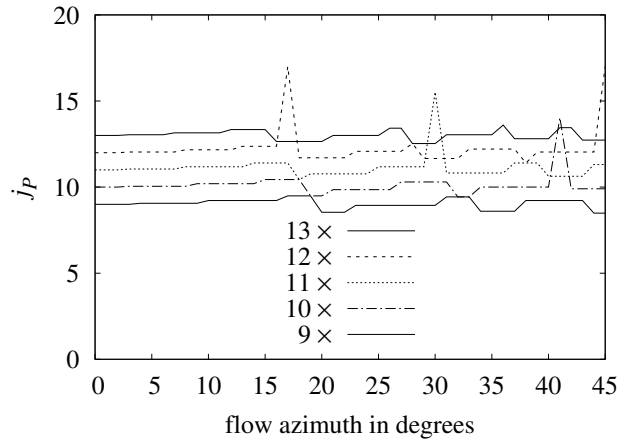


Figure 12 bi-level plate 25%

Figure 11 shows the j_P values for a square equal-area bi-level surface (regular array of square posts on a flat plate) computing $X_{j,k}$ from a 64×64 interpolated sampling of that surface with azimuth from 0° through 45° , and which is scaled between 9 and 13 cells on a side. At each scale, j_P varies within a ± 1 range versus the azimuth. Figure 12 shows a 25% high, 75% low, bi-level surface; its j_P has peaks outside of the ± 1 range. This suggests a quantitative criterion for surface roughness isotropy:

A surface roughness is isotropic if j_P varies no more than ± 2 through its full rotation.

More specifically, using $w \times w$ ($w \geq 64$) samplings of roughness at nine scales over a 2:1 range such that most of the calculated j_P values satisfy $8 \leq j_P \leq 16$ at each scale, do 56 sampling trials with randomized offset and randomized azimuth rotation per scale. A roughness is considered isotropic if no more than 5 of the $504 (= 56 \times 9)$ trials have j_P varying more than $\pm w/32$ from its scale.

Using this criterion, square post arrays having upper area fraction between 27% and 76% are isotropic. Square arrays of circular columns having upper area fraction between 24% and 78% are isotropic. Hexagonal arrays of circular columns having upper area fraction between 6% and 75% are isotropic. Swapping the elevations, hexagonal arrays of circular depressions in a flat plate having upper area fraction between 25% and 94% are isotropic.

Plates with 15% elongated hexagonal arrays of cone or bump protrusions described in Schlichting [5] are also isotropic; L_P is near the geometric mean of the periods of the elongated axis and its perpendicular.

The visual appearance of isotropy and this test for isotropy are not equivalent. Square post arrays having upper area fractions of 20% do not pass the isotropy test, while those with 30% do. Plates from Schlichting [5] having elongated hexagonal arrays of cones are not visually isotropic, but pass this isotropy test.

12. Onset of rough turbulence

For an isotropic, periodic roughness with $0 < \varepsilon < L_P \ll L$, there must be some value $Re_\lambda > 0$ such that when $0 < Re < Re_\lambda$, the fluid flow exhibits laminar or smooth turbulent behavior along the entire plate.

The boundary-layer is thinnest at the leading edge. Because its roughness is periodic, any disruption will start within the leading band ($0 < x < L_P$) of roughness. In this investigation, a boundary-layer is considered disrupted when $\varepsilon > \delta_2(L_P)$, where $\delta_2(x)$ is the boundary-layer momentum thickness at x .

$\delta_2(x)$ is the thickness of bulk flow having the same momentum flow rate as the plate boundary-layer at x . Momentum thickness δ_2 is not a directly measurable quantity. Schlichting [9] gives the momentum thickness of laminar and smooth turbulent boundary-layers as $\delta_{2\lambda}(x) = 0.664 x Re_x^{-1/2}$ and $\delta_{2\sigma}(x) = 0.036 x Re_x^{-1/5}$, respectively. Equivalently, the laminar and smooth turbulent boundary-layer thicknesses are:

$$\delta_{2\lambda}(x) = 0.664 \sqrt{Re_x} \frac{L}{Re} \quad \delta_{2\sigma}(x) = 0.036 Re_x^{4/5} \frac{L}{Re} \quad (35)$$

The laminar $\delta_{2\lambda}$ is from the Blasius boundary-layer model, which is well supported by measurement. The smooth turbulent $\delta_{2\sigma}$ formula is less certain.

The smooth turbulence momentum thickness $\delta_2(x)$ is a local property of the fluid flow. In order to work with the roughness Reynolds number Re_ε locally, substitute x for L and Re_x for Re in formula (28) and solve $Re_\varepsilon = 1$ for x/ε :

$$Re_\varepsilon = \frac{Re_x}{\sqrt{3} [x/\varepsilon] \ln(x/\varepsilon)} = 1 \quad \frac{Re_x}{\sqrt{3}} = \frac{x}{\varepsilon} \ln \frac{x}{\varepsilon} \quad \frac{x}{\varepsilon} = \exp \left(W_0 \left(\frac{Re_x}{\sqrt{3}} \right) \right) \quad (36)$$

Re_x grows proportionally to x ; hence, the smooth turbulence momentum thickness $\delta_2(x)$ should be proportional to the product of x and formula (24), the ratio of friction travel to run travel:

$$\delta_2(x) \propto \frac{x}{\sqrt{3} \ln(x/\varepsilon)} = \frac{x}{\sqrt{3} W_0(Re_x/\sqrt{3})} \quad (37)$$

The coefficient seems to be $1/3^3 \equiv 1/27 \approx 0.0370$, which is close to the $\delta_{2\sigma}$ coefficient, 0.036:

$$\delta_2(x) = \frac{x}{3^3 W_0(Re_x/\sqrt{3})} \quad Re_x \gg \sqrt{3}e \quad (38)$$

The occurrence of 3^3 may be related to $\exp(\varphi \ln(\varphi)) \equiv \varphi^\varphi$.

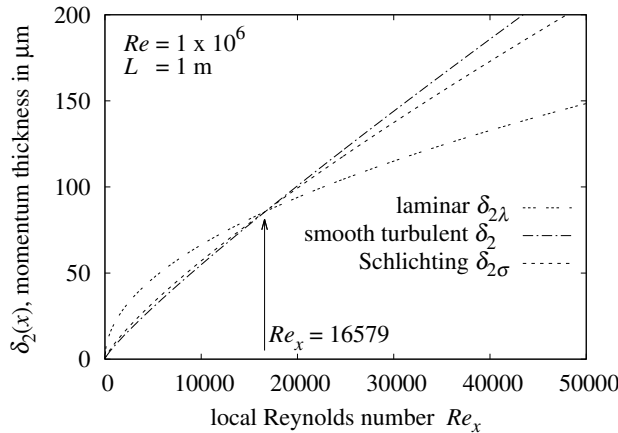


Figure 13 smooth plate $\delta_2(x)$ versus Re_x

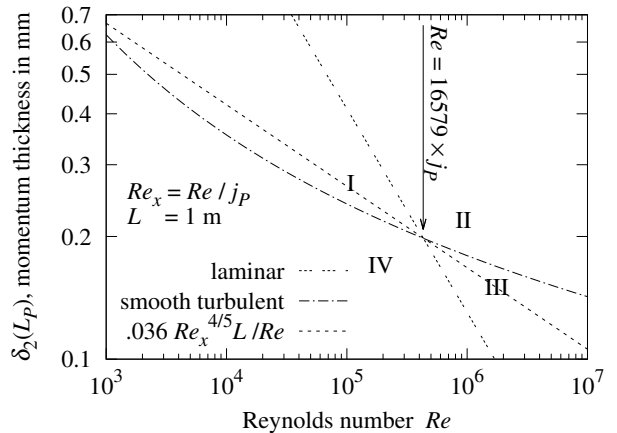


Figure 14 smooth plate $\delta_2(L_P)$ versus Re

Figure 13 demonstrates that “smooth turbulent δ_2 ” from equation (38) and $\delta_{2\sigma}$ from equation (35) are close to each other between the origin and the intersection of the laminar and turbulent curves at:

$$0.664 \sqrt{Re_x} = 0.036 Re_x^{4/5} \quad Re_x = \left[\frac{0.664}{0.036} \right]^{10/3} \approx 16579 \quad (39)$$

When $x = L_P \ll L$, then $Re_x \ll Re$; hence, $\delta_{2\sigma}(L_P)$ is a reasonable approximation for $\delta_2(L_P)$ in the leading band of roughness.

Figure 14 shows the (theoretical) momentum thickness of laminar and smooth turbulent flows along a 1 m long plate versus Re . The laminar $\delta_{2\lambda}$ and smooth turbulent δ_2 curves divide the graph into four regions. When the point at coordinates $[Re, \varepsilon]$ is in regions I or IV, then ε is not high enough to significantly disrupt laminar flow; hence, leading band fluid flow will be laminar (possibly becoming smooth turbulent downstream). When $[Re, \varepsilon]$ is in region II, then its height is sufficient to disrupt both laminar and smooth turbulent flow; hence, fluid flow along the plate will be rough turbulent.

When $[Re, \varepsilon]$ is in region III, then the roughness would be sufficient to disrupt laminar flow, but not large enough to disrupt smooth turbulent flow; hence, leading band fluid flow would be smooth turbulent.

With $\delta_{2\lambda} = \varepsilon$ and $x = L_P$, solve $\delta_{2\lambda}$ formula (35) for the laminar upper-bound Re_λ :

$$Re_\lambda = \left[\frac{0.664}{\varepsilon} \right]^2 L_P L \quad (40)$$

With $x = L_P$ and $\delta_2(x) = \varepsilon$ in formula (38):

$$\varepsilon = \frac{L_P}{3^3 W_0 (Re L_P / (\sqrt{3} L))} \quad W_0 \left(\frac{Re L_P}{\sqrt{3} L} \right) = \frac{L_P}{3^3 \varepsilon} \quad Re \gg \frac{\sqrt{3} \varepsilon L}{L_P} \quad (41)$$

The inverse of $\varphi = W_0(\vartheta)$ is $\vartheta = \varphi \exp(\varphi)$. Solving for $Re_\sigma = Re$:

$$\frac{Re L_P}{\sqrt{3} L} = \frac{L_P}{3^3 \varepsilon} \exp \frac{L_P}{3^3 \varepsilon} \quad Re_\sigma = \frac{\sqrt{3} L}{3^3 \varepsilon} \exp \frac{L_P}{3^3 \varepsilon} \quad (42)$$

Equating Re_λ and Re_σ yields their intercept (found numerically):

$$0.664^2 \frac{L_P}{\varepsilon} = \frac{\sqrt{3}}{3^3} \exp \frac{L_P}{3^3 \varepsilon} \quad \frac{L_P}{\varepsilon} \approx 194.3 \quad (43)$$

To reach region III requires a plate with repeated relative roughness $L/\varepsilon > 20 L_P/\varepsilon \approx 3886$. Machining precision must be much finer than this in order for the roughness of each patch to be significantly larger than the residual elevation error. Region III smooth turbulent flow will be rare; most plates with periodic roughness will transition directly from laminar to rough turbulent flow as Re surpasses Re_λ .

13. Flat-peaked roughness

Section 12 explored flow modes involving the entire periodically rough surface. Mixed flow modes can form along plates whose peaks of the roughness are all co-planar (at the same elevation) flats. At flows large enough to produce rough turbulence in the leading band of the plate, smooth turbulent flow occurs downwind from where x is large enough for the boundary layer (which grows with x) to bridge the gaps. The drag from the downwind portion of such a surface will be proportional to $\overline{f_{c\sigma}}$, not the constant coefficient $\overline{f_c}$ of rough turbulent flow; this makes it an instance of a non-constant terminal drag coefficient as described by S. F. Hoerner in Hama [6] (see present work Section 1).

Let a “flat-peaked roughness” be an isotropic, periodic roughness where each cell contains a contiguous flat-peak area whose boundary has a convex perimeter within the cell, and all the flat-peak areas are at the same elevation. This will either be an array of “islands” whose tops are all co-planar, or an array of “wells” dropping below an otherwise flat plane.

Consider a smooth flat plate etched with a square grid of grooves subjected to a moderate flow parallel to its surface. When the boundary-layer is disrupted by a groove perpendicular to the flow, the smooth turbulent boundary-layer restarts at the leading edge of the flat-peak. At the scale of the roughness period L_P , the momentum thickness of the boundary-layer grows from 0 to nearly the L -scale $\delta_2(x)$ value (depending on how long the flat is). If it grows to exceed ε , then the rest of the plate (to its trailing edge) will have a smooth turbulent skin-friction coefficient proportional to $\overline{f_{c\sigma}}$.

For isotropic roughness, the growth of δ_2 depends on the size of the flat-peaks, but not on their orientation with respect to the flow. In natural convection from an upward-facing horizontal plate [22, 23], the isotropic characteristic-length metric L^* is the ratio of the convex region area to its perimeter. For a regular polygon or circle, $L^* = r/2$, where r is the minimum radius of the regular polygon or circle.

Multiplying both sides of δ_2 formula (38) by $3^3 Re/(\sqrt{3} L)$ allows Re_x to be isolated using the Lambert W_0 function identity $\varphi/W_0(\varphi) = \exp W_0(\varphi)$:

$$\frac{3^3 Re}{\sqrt{3} L} \delta_2 = \frac{Re_x/\sqrt{3}}{W_0(Re_x/\sqrt{3})} = \exp W_0\left(\frac{Re_x}{\sqrt{3}}\right) \quad (44)$$

Let $\delta_2 = \varepsilon$ in order to find the island Re_x threshold Re_I . Turning to dimensional analysis, the Re strength needed to produce smooth turbulence grows with ε/L^* and with L/L_P . Substituting a product of powers of these ratios for Re in equation (44), then taking the logarithm of both sides:

$$Re = \frac{\varepsilon}{L^*} \left[\frac{L}{L_P}\right]^3 \ln \frac{3^3 \varepsilon^2 L^2}{\sqrt{3} L^* L_P^3} = W_0\left(\frac{Re_x}{\sqrt{3}}\right) \quad (45)$$

The inverse of $\varphi = W_0(\vartheta)$ is $\vartheta = \varphi \exp(\varphi)$:

$$Re_I = Re_x = \frac{3^3 \varepsilon^2 L^2}{L^* L_P^3} \ln \frac{3^3 \varepsilon^2 L^2}{\sqrt{3} L^* L_P^3} \frac{[4 L^*]^2}{L_P^2} > \frac{1}{2} \quad (46)$$

With large enough gaps, the islands are too short to support smooth turbulence bridging the gaps, leading to the inequality. Formula (46) is tested against a square-grooved plate in Section 23.

When a perforated sheet is laid on a flat plate, the holes in the sheet become wells. L^* is the ratio of the hole area to its perimeter. Fluid flow along the perforated sheet must return to the upper level after diving into a well; hence, there are twice as many roughness interactions per cell. Instead of $Re = [\varepsilon/L^*] [L/L_P]^3$ in formula (45), let:

$$Re = \frac{\varepsilon}{L^*} \left[\frac{L}{2 L_P}\right]^3 \ln \frac{3^3 \varepsilon^2 L^2}{\sqrt{3} 2^3 L^* L_P^3} = W_0\left(\frac{Re_x}{\sqrt{3}}\right) \quad (47)$$

leading to the wells Re_x threshold Re_W :

$$Re_W = Re_x = \frac{3^3 \varepsilon^2 L^2}{2^3 L^* L_P^3} \ln \frac{3^3 \varepsilon^2 L^2}{\sqrt{3} 2^3 L^* L_P^3} \frac{[4 L^*]^2}{L_P^2} < \frac{1}{2} \quad (48)$$

With large enough wells, the flats between them are too narrow to support smooth turbulence bridging the wells, leading to the inequality. Formula (48) is tested against perforated sheets in Section 22.

For a flat-peaked roughness, let “openness” $0 < \Omega < 1$ be the ratio of the non-peak area to the cell area; $1 - \Omega$ will thus be the ratio of the peak area to the cell area. Let $S_{s,t}$ be a $w \times w$ matrix of elevations from Section 11. The span of elevations accepted as flat-peaked must be small, have length units, and involve ε and L_P , which suggests ε^3/L_P^2 :

$$\Omega \approx \frac{1}{w^2} \sum_{t=0}^{w-1} \sum_{s=0}^{w-1} \begin{cases} 1, & \text{if } S_{s,t} < \max(S) - \varepsilon^3/L_P^2; \\ 0, & \text{otherwise.} \end{cases} \quad (49)$$

For flat-peaked islands and wells, with convex area A^* and perimeter length p^* , $L^* = A^*/p^*$. Because L_P is the isotropic period, the effective cell area $A_P = \pi L_P^2/4$.

$$\frac{1}{2} < \frac{[4 L^*]^2}{L_P^2} = \frac{A^*}{A_P} \frac{4 \pi A^*}{p^{*2}} = [1 - \Omega] o \quad \Omega < 1 - \frac{1}{2o} \quad (50)$$

$$\frac{1}{2} > \frac{[4 L^*]^2}{L_P^2} = \frac{A^*}{A_P} \frac{4 \pi A^*}{p^{*2}} = \Omega o \quad \Omega < \frac{1}{2o} \quad (51)$$

Circularity $o = 4 \pi A^*/p^{*2} = 4 \pi L^{*2}/A^*$ takes its maximum value, 1, for a disk; it is $\pi\sqrt{3}/6 \approx 0.907$ for a hexagon, $\pi/4 \approx 0.785$ for a square, and $\pi\sqrt{3}/9 \approx 0.605$ for an equilateral triangle.

Criteria (50) and (51) can replace the inequalities in formulas (46) and (48), respectively.

All of the flat-peaked roughness measurements cited or performed by this investigation were from plates having bi-level roughness.

14. Local skin-friction

Conversions between local and average skin-friction are needed in order to compare prior with present work.

The ratio of average to local skin-friction $\overline{f_{c\sigma}}/f_{c\sigma} > 1$ of a continuous boundary-layer is calculated from $f_{c\sigma}$ by formula (52). The singularity (division by 0) at the leading edge of the plate is avoided by using $Re_0 > 0$ as the integration lower bound; Re_0 must be chosen such that $f_{c\sigma}(Re_0) \ll 1$.

$$\frac{\overline{f_{c\sigma}}(Re)}{f_{c\sigma}(Re)} = \frac{1}{Re - Re_0} \int_{Re_0}^{Re} \frac{f_{c\sigma}(Re_x)}{f_{c\sigma}(Re)} dRe_x \quad (52)$$

The local skin-friction coefficient f_c is not well-defined for self-similar roughness because its L/ε is constant. Periodic roughness has varying L/ε ; it also provides L_P/ε as the lower-bound of integration.

A crucial difference between periodic roughness and smooth surfaces is that periodic roughness disrupts the boundary-layer repeatedly. Thus, the local skin-friction coefficients being averaged are independent; instead of $\overline{f_c}/f_c$ accruing linearly, it should go as the square:

$$\frac{\overline{f_c}(L/\varepsilon)}{f_c(L/\varepsilon)} = \left[\frac{\varepsilon}{L - L_P} \int_{L_P/\varepsilon}^{L/\varepsilon} \frac{f_c(r)}{f_c(L/\varepsilon)} dr \right]^2 \quad (53)$$

Applying formula (53) to the Mills-Hang local formula (9) yields the average skin-friction coefficient:

$$\overline{C_f}^2 / C_f \quad (54)$$

where C_f and $\overline{C_f}$ are from equations (9) and (10), respectively.

At $L/\varepsilon = 4000$ ($L/k_S = 750$), formula (54) has values in excess of 20% larger than the Mills-Hang $\overline{C_f}$ formula (10) derived using averaging formula (13). The average skin-friction coefficient was of minor importance in Mills and Hang [8]; the paper did not do comparisons with measurements of average skin-friction.

For disrupted boundary-layers, the transform for local friction f_c given average friction $\overline{f_c}$ is:

$$\frac{f_c(L/\varepsilon)}{\overline{f_c}(L/\varepsilon)} = \left[\frac{d([L - L_P] \overline{f_c}(L/\varepsilon))}{dL} / \overline{f_c}(L/\varepsilon) \right]^2 \quad (55)$$

Applying formula (55) to $\overline{f_c}$ formula (27) for rough surfaces yields the local skin-friction coefficient:

$$f_c(x/\varepsilon) = \frac{1}{3} \left[\frac{\ln(x/\varepsilon) + 2[L_P/x - 1]}{\ln^2(x/\varepsilon)} \right]^2 \quad L \geq x > L_P \geq \varepsilon \quad (56)$$

The local skin-friction coefficient for smooth turbulent flow $f_{c\sigma}$ can be derived from $\overline{f_{c\sigma}}$ equation (31) and equations (57) provided that $Re_x \geq Re_0 \geq \sqrt{3}e$ and $Re_x \gg \sqrt{3}e$:

$$\frac{dW_0(\vartheta)}{d\vartheta} = \frac{W_0(\vartheta)}{\vartheta [W_0(\vartheta) + 1]} \quad f_{c\sigma}(Re_x) = \frac{d([Re_x - Re_0] \overline{f_{c\sigma}}(Re_x))}{dRe_x} \quad (57)$$

$$f_{c\sigma}(Re_x) = \frac{\sqrt[3]{2} W_0^2(Re_x/\sqrt{3}) - 2[1 - Re_0/Re_x] W_0(Re_x/\sqrt{3}) - 1}{3 [W_0(Re_x/\sqrt{3}) - 1]^3 [W_0(Re_x/\sqrt{3}) + 1]} \quad (58)$$

Figure 15 plots local smooth turbulent skin-friction coefficient formulas and measurements collected in Churchill [11]. The measurements have 1.9% RMSRE from “present work” formula (58).

Note that when calculating RMSRE, the error due to variation at a single point is larger than the error when that variation is split among multiple points. Thus, local measurements tend to have larger RMSRE than average measurements. In Figure 15, the primary error contributor is the value at $Re_x = 10^7$.

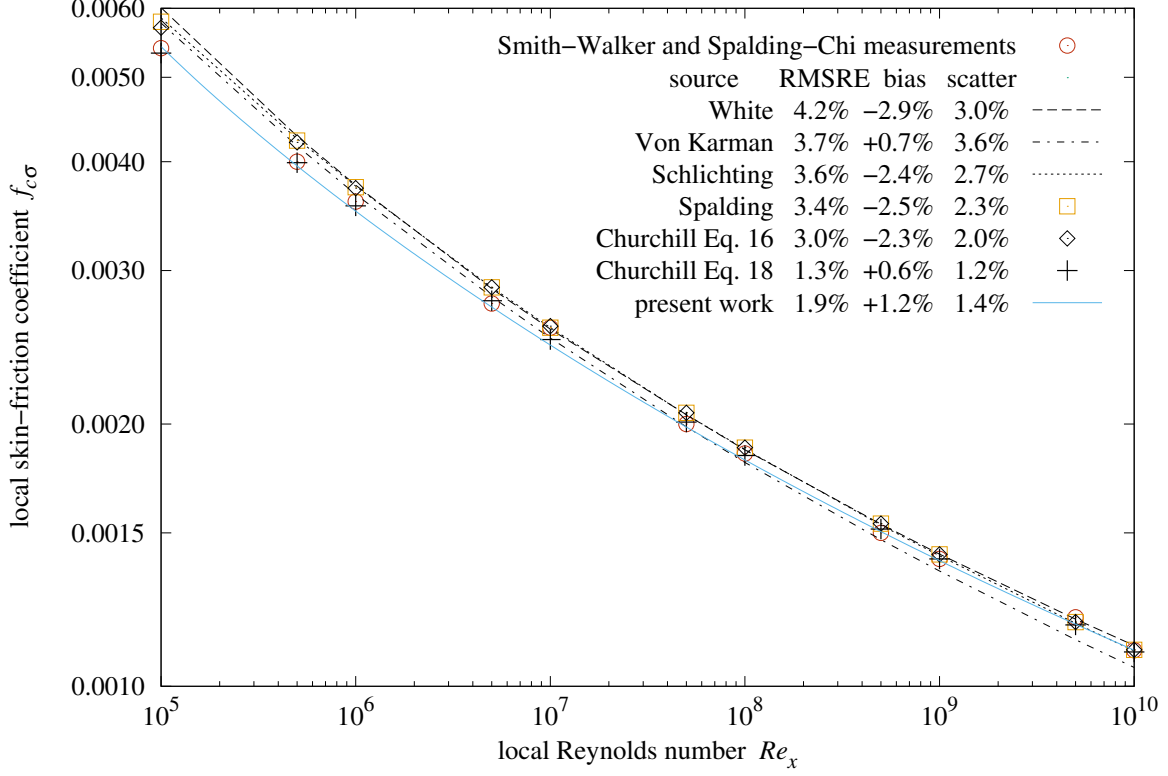


Figure 15 local $f_{c\sigma}$ versus Re_x of smooth plate

15. Forced convection from a rough plate

Forced convective heat transfer is expressed as the dimensionless average (\overline{Nu}) or local (Nu) Nusselt number. Heat transfer by rough turbulence will grow with the amount of turbulence induced, $\overline{f_c} Re$. It will also grow with $\sqrt[3]{Pr}$. The fluid's Prandtl number (Pr) is the ratio of kinetic viscosity to thermal diffusivity. Fluids with large Pr transport heat in the fluid flow; conduction is dominant in fluids with small Pr . The $1/3$ exponent for Pr may relate to it being a property of the fluid in three dimensions. Heat transfer from the trailing part of the plate is reduced due to fluid heating by the leading part; hence, convection will be scaled by $1/2$. Expanding $\overline{f_c}$ from equation (27) yields formula (59) for rough turbulent average forced convection:

$$\overline{Nu} = \frac{\overline{f_c} Re Pr^{1/3}}{2} = \frac{Re Pr^{1/3}}{6 \ln^2(L/\varepsilon)} \quad \frac{L}{\varepsilon} \gg 1 \quad Pr > 0 \quad (59)$$

The present analysis for self-similar $\overline{f_c}$ did not involve boundary-layers; hence, it avoids the $Pr > 0.6$ restriction affecting formula (60). Formula (59) is compared with measurements in Section 23.

16. Forced convection from a smooth plate

For smooth turbulent convection, Lienhard [24] recommends composing the Gnielinski formula (60) with the White smooth formula (12) for $C_{f\sigma}$. Note that formula (60) is local convection (Nu).

$$Nu = \frac{Re_x Pr C_{f\sigma}/2}{1 + 12.7 [Pr^{2/3} - 1] \sqrt{C_{f\sigma}/2}} \approx \frac{Re_x Pr C_{f\sigma}/2}{1 + 9 [Pr^{2/3} - 1] \sqrt{C_{f\sigma}}} \quad Pr \geq 0.6 \quad (60)$$

Lienhard states that Nu formula (61) has similar accuracy for gases:

$$Nu = 0.0296 Re_x^{4/5} Pr^{0.6} \quad \overline{Nu} = 0.037 Re^{4/5} Pr^{0.6} \quad (61)$$

Forced convection is similar to natural convection from a vertical plate; in both, fluid flows parallel to the plate's characteristic-length axis, and is uniform across the plate's other axis.

Jaffer [25] finds that stationary fluid conducts heat from the plate with an effective Nusselt number Nu_0 , which is a coefficient factor of both the static and flow-induced heat transfer terms:

$$Nu_0 = \frac{2^4}{\pi^2 \sqrt[4]{2}} \approx 1.363 \quad (62)$$

Flow-induced heat transfer grows with $Nu_0 Re \sqrt{f_{c\sigma}}$. Because this heat traverses boundary-layers, the Pr dependence is more complicated than $\sqrt[3]{Pr}$. In Jaffer [25], the vertical-plate natural convection dependence is $\sqrt[3]{Pr/\Xi(Pr)}$, where $\Xi(Pr)$ is defined using ℓ^p -norm definition (63) with $p = \sqrt{1/3}$:

$$\|\varphi, \vartheta\|_p \equiv (|\varphi|^p + |\vartheta|^p)^{1/p} \quad (63)$$

$$\Xi(Pr) = \left\| 1, \frac{0.5}{Pr} \right\|_{\sqrt{1/3}} \quad (64)$$

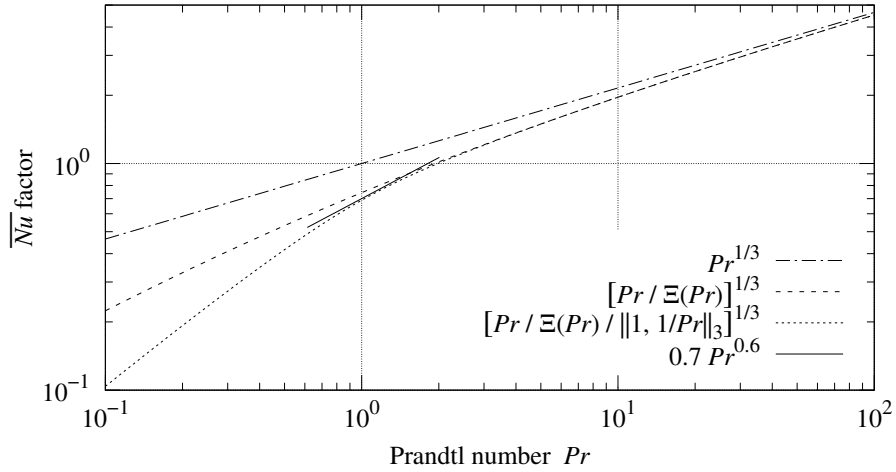


Figure 16 smooth plate \overline{Nu} dependence on Pr

In Figure 16, $\sqrt[3]{Pr/\Xi(Pr)}$ is asymptotically $\sqrt[3]{Pr}$ for large Pr and $\sqrt[3]{2} Pr^{2/3}$ for small Pr . At small Pr , conduction does not amplify forced convection as it does for natural convection; the Pr exponent should be 1. An additional factor using the ℓ^3 -norm accomplishes this. Formula (65) is asymptotically $\sqrt[3]{2} Pr$ for $Pr < 0.5$. The “ $0.7 Pr^{0.6}$ ” trace shows that formula (65) has a slope close to formula (61) for gases.

$$\sqrt[3]{\frac{Pr}{\Xi(Pr)}} \sqrt[3]{\frac{1}{\|1, 1/Pr\|_3}} \quad (65)$$

The slope of formula (60) $Nu(Re_x)$ decreases with increasing Pr ; for large Pr , $Nu \propto \sqrt{C_{f\sigma}}$. Recall from equations (25) and (26) that $\overline{f_c} \propto u_\tau^2$; hence $\sqrt{\overline{f_c}} \propto u_\tau$. This indicates that transport through the boundary-layer limits convection at large Pr . In order to reduce the asymptotic dependence from $\overline{f_{c\sigma}}$ to $\sqrt{\overline{f_{c\sigma}}}$, the convection formula will include a factor which takes square-root of an expression gating $\overline{f_{c\sigma}}$ by Pr :

$$\sqrt{\overline{f_{c\sigma}}} \sqrt{\frac{Pr/\sqrt{162} + 1}{\sqrt{162} Pr + 1/\overline{f_{c\sigma}}}} \quad \sqrt{162} = 9\sqrt{2} \approx 12.7 \quad (66)$$

The scaling for upstream heating was $1/2$ in formula (59) for disruptive roughness; the smooth turbulent boundary-layer reduces this interaction; $\sqrt{1/3} \approx 0.577$ appears correct in the smooth case.

Formula (67) is proposed for smooth turbulent convection for all $Pr > 0$:

$$\overline{Nu}_\sigma = \frac{Nu_0 Re}{\sqrt{3}} \sqrt{\frac{\overline{f_{c\sigma}} [Pr/\sqrt{162} + 1]}{\sqrt{162} Pr + 1/\overline{f_{c\sigma}}}} \sqrt[3]{\frac{Pr/\Xi(Pr)}{\|1, 1/Pr\|_3}} \quad Re \gg \sqrt{3} e \quad (67)$$

Lienhard [24] compares the Gnielinski-White convection formula with local measurements from studies of a variety of fluids with $0.7 \leq Pr \leq 257$ spanning $4000 < Re_x < 4.3 \times 10^6$. The smallest turbulent Re_x presented was $\approx 10^5$. Note that formula (61) is more accurate than Gnielinski-White for turbulent air ($Pr \approx 0.71$) at $Re_x < 10^5$.

Figures 17 and 18 show \overline{Nu} versus Pr and Re , respectively. The “present work” traces are formula (67). The “Lienhard” traces use formula (68) to numerically average the composition of the Gnielinski formula (60) with the White formula (12). Note that formula (68) is different from the f_c transforms in Section 14.

$$\overline{Nu}(Re) = \int_{Re_0}^{Re} \frac{Nu(Re_x)}{Re_x} dRe_x \quad (68)$$

Formula (67) \overline{Nu}_σ matches the numerically averaged Gnielinski-White formula within $\pm 6.6\%$ over the range $10^5 < Re < 4.3 \times 10^6$ with $4.0 \leq Pr \leq 257$. At $Pr = 0.71$, \overline{Nu}_σ matches formula (61) \overline{Nu} within $\pm 4\%$ over the range $10^4 < Re < 4.3 \times 10^6$.

$$Nu_\sigma = Re_x \frac{d\overline{Nu}_\sigma(Re_x)}{dRe_x} \quad (69)$$

Over the same ranges, local convection Nu_σ formula (69) matches formulas (60) and (61) within $\pm 7.1\%$. Figure 19 shows Nu_σ and Gnielinski formula (60) versus Re_x .

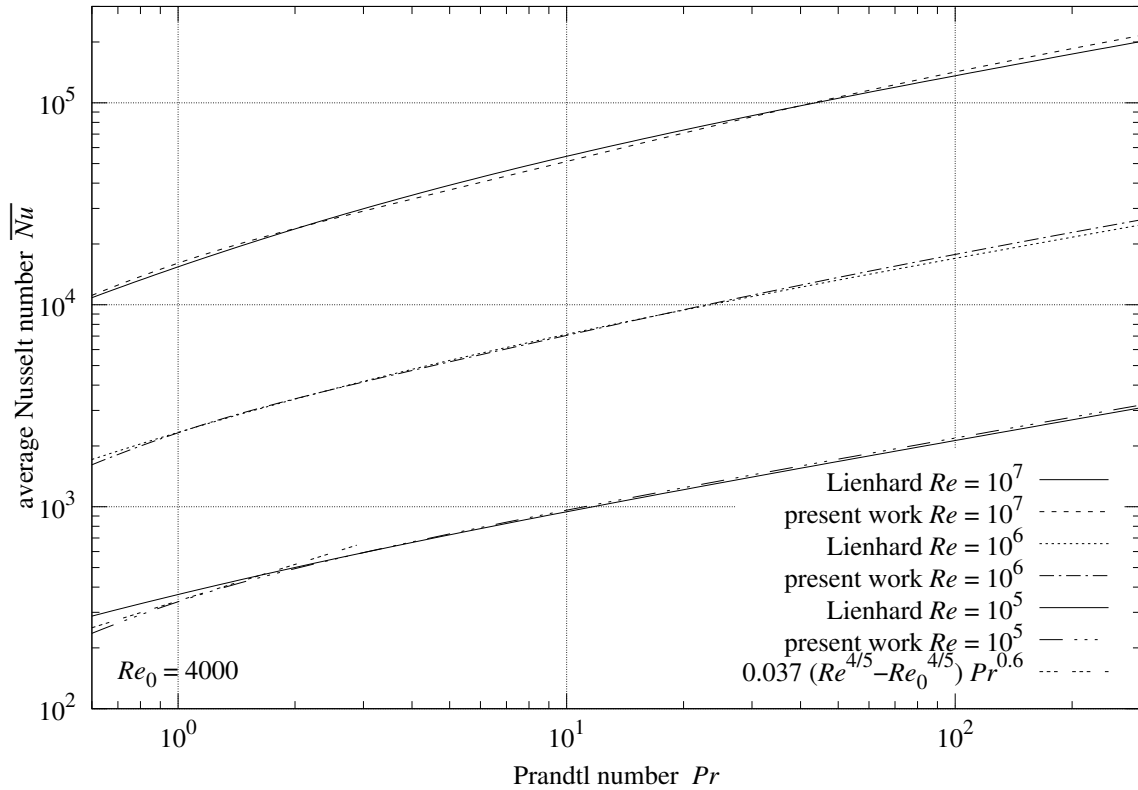


Figure 17 smooth plate average turbulent convection versus Pr

Adapting the Lienhard [24] comprehensive smooth plate convection formula to use Nu_σ formula (69):

$$Nu(Re_x) = \left\| \left\| Nu_\lambda(Re_x), \left\| \left[\frac{Re_x}{Re_l} \right]^c Nu_\lambda(Re_l), Nu_\sigma(Re_x) \right\|_{-10} \right\|_5 \quad (70)$$

$$Nu_\lambda(Re_x) = 0.332 \sqrt{Re_x} Pr^{1/3} \quad c = 0.9922 \log_{10} Re_l - 3.013$$

where $Re_l < 2.8 \times 10^6$ is the plate-specific upper-bound for purely laminar flow. For a periodic roughness with $Re_\sigma < Re_\lambda$, the purely laminar upper-bound $Re_l = Re_\sigma$.

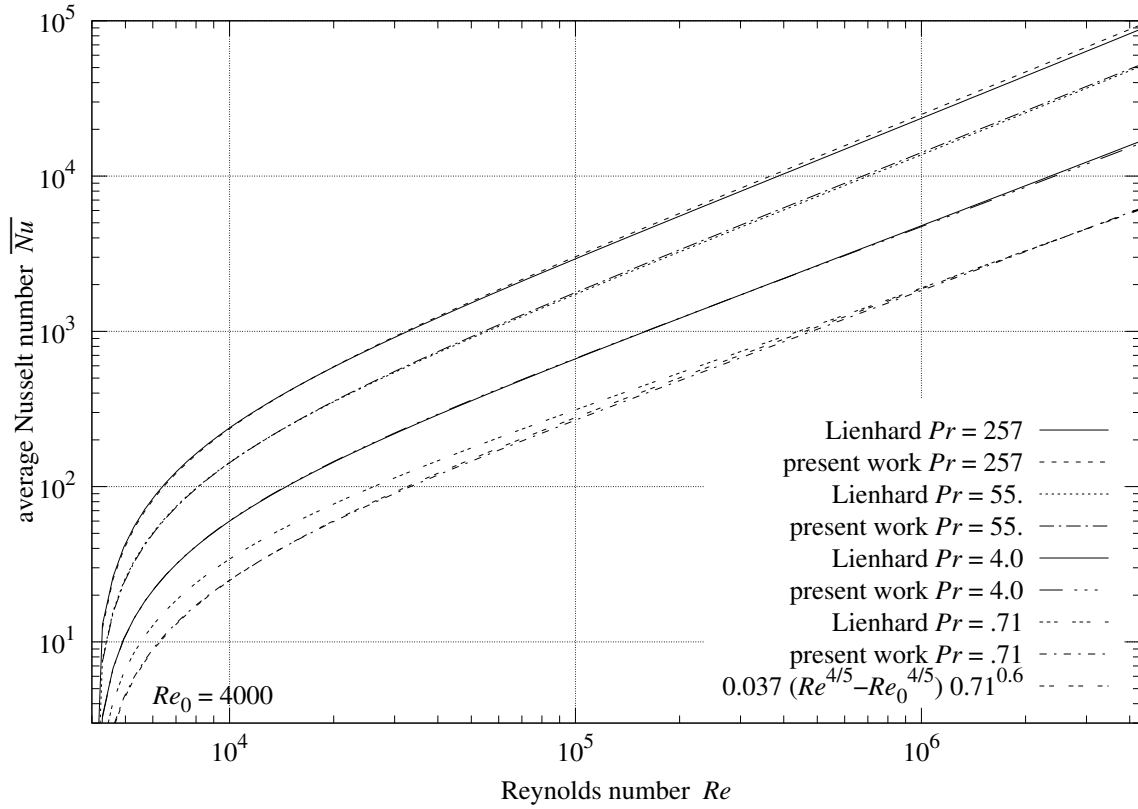


Figure 18 smooth plate average turbulent convection versus Re

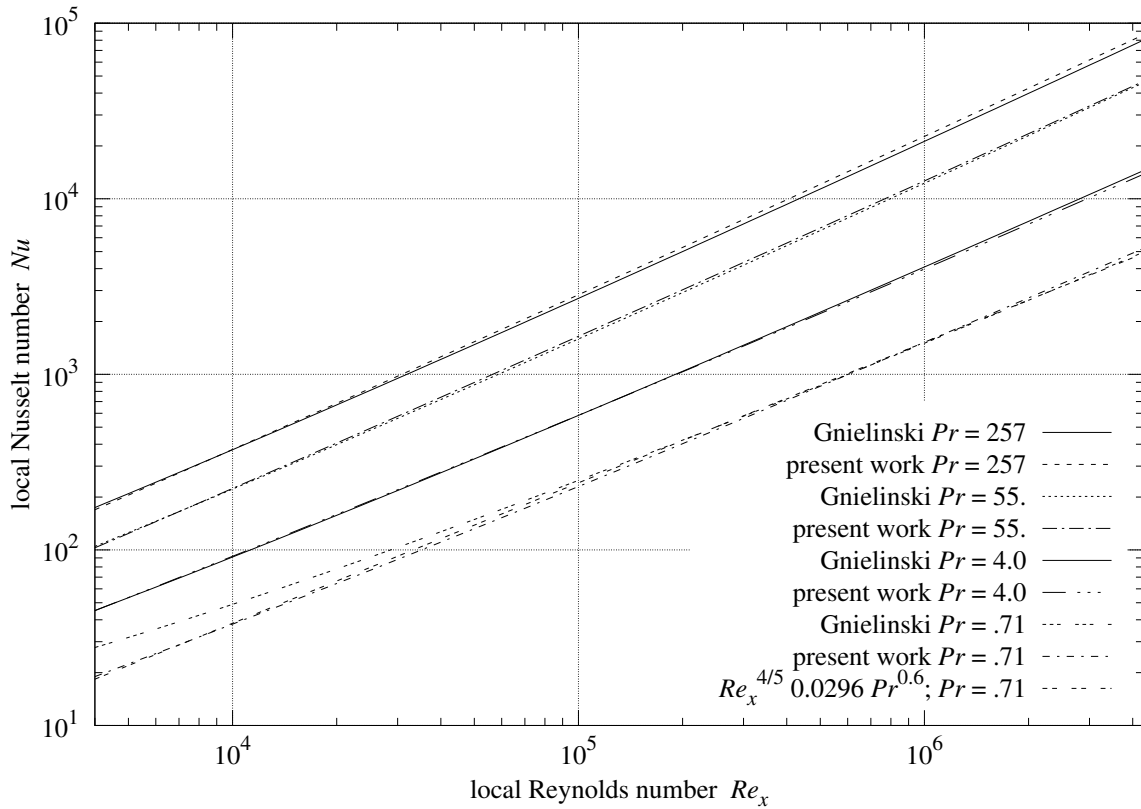


Figure 19 smooth plate local turbulent convection versus Re_x

17. Periodic smoothness and laminar flow

A perfectly flat single-crystal silicon wafer should behave as predicted by formula (70), the comprehensive smooth surface formula from Lienhard [24]. At atomic scale however, the wafer is a periodic, isotropic roughness with $L_p = 543$ nm, $\varepsilon = 31.2$ nm, and $L = 30.5$ cm.

The amount of fluid displaced by roughness in a laminar flow grows with both ε and L_p . The Reynolds number where this displacement becomes significant is the ratio of length scales $L/\sqrt{\varepsilon L_p}$.

	L/L_p	L/ε	$L/\sqrt{\varepsilon L_p}$	Re_σ	Re_λ
silicon wafer	5.62×10^5	9.78×10^6	2.34×10^6	$> 1.19 \times 10^6$	$\ll 7.50 \times 10^7$
cloth tape (dull)	1.32×10^2	8.82×10^3	1.08×10^3	$< 6.70 \times 10^3$	$\ll 2.59 \times 10^5$
cloth tape (shiny)	1.54×10^2	7.08×10^3	1.04×10^3	$< 2.49 \times 10^3$	$\ll 1.43 \times 10^5$
Pimenta et al	1.72×10^3	1.47×10^4	5.02×10^3	$> 1.29 \times 10^3$	$\ll 5.51 \times 10^4$
1 mm bi-level	2.60×10^1	2.96×10^2	8.77×10^1	$> 2.89 \times 10^1$	$\ll 1.48 \times 10^3$
3 mm bi-level	2.60×10^1	1.02×10^2	5.14×10^1	$> 7.55 \times 10^0$	$\ll 1.76 \times 10^2$

Table 2 dimensionless parameters

Table 2 shows dimensionless parameters for plates with various surfaces. All the plates have $Re_\sigma < Re_\lambda$; the present theory predicts that rough turbulence will start in the leading band of roughness when $Re > Re_\lambda$.

Isotropic, periodic plates with $L/\sqrt{\varepsilon L_p} > Re_\sigma$ can be considered “smooth”, behaving as formula (70) within the range $Re < Re_\lambda$. The Re_x value where $\delta_2(Re_x) = \varepsilon$ is Re_σ ; it is used for Re_l in formula (70).

If $L/\sqrt{\varepsilon L_p} < Re_\sigma$, the roughness perturbs laminar flow enough to spawn some smooth turbulence, but not enough to force it into rough turbulence. This suggests treating the forced convection \overline{Nu} as competition between laminar convection \overline{Nu}_λ and smooth turbulent convection \overline{Nu}_σ .

If the laminar and turbulent flows were perpendicular, their convection processes would combine as the ℓ^2 -norm (formula (63) with $p = 2$). But these flows are in the same direction. Independent processes combine as the ℓ^1 -norm (addition); but these processes are competitive, not independent. An intermediate strength is needed. The geometric mean of 1 and 2 is $\sqrt{2}$; hence, the $\ell^{\sqrt{2}}$ -norm is proposed for this mild competition:

$$\overline{Nu}(Re) = \|\overline{Nu}_\lambda(Re), \overline{Nu}_\sigma(Re)\|_{\sqrt{2}} \quad \overline{Nu}_\lambda(Re) = 0.664 \sqrt{Re} Pr^{1/3} \quad (71)$$

\overline{Nu}_λ combines the Blasius laminar model with the Colburn [26] analogy. Formula (71) is tested in Section 24.

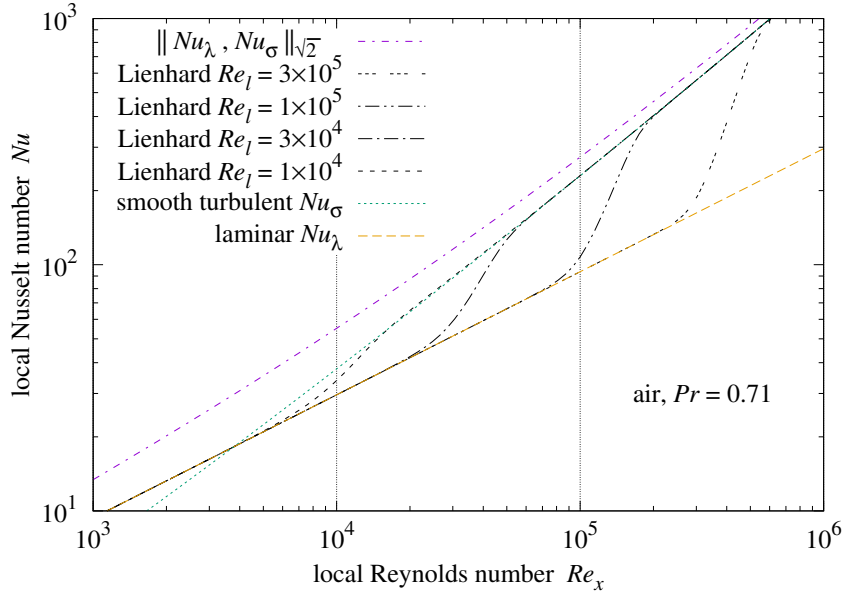


Figure 20 laminar to smooth turbulent convection transitions

Figure 20 shows the local forced convection Nu , calculated by applying formula (69) to \overline{Nu} formula (71); it is indistinguishable from $\|\overline{Nu}_\lambda(Re_x), \overline{Nu}_\sigma(Re_x)\|_{\sqrt{2}}$ at the scale of Figure 20. Also shown is formula (70) at four Re_l values, along with pure smooth turbulent and pure laminar convections.

18. Turbulent flow modes

Fluid flow along isotropic, periodic roughness can be multi-modal when it is flat-peaked roughness.

condition	flat-peaked islands	flat-peaked wells
$[4L^*]^2/L_P^2 < 1/2$	rough formulas (27, 56, 59)	
$Re_x < Re_I$	rough formulas (27, 56, 59)	
$Re_x > Re_I$	smooth formula (72)	
$[4L^*]^2/L_P^2 > 1/2$		rough formulas (27, 56, 59)
$Re_x < Re_W$		mix formula (73)
$Re_x > Re_W$		smooth formula (74)

Table 3 turbulent flow modes for flat-peaked roughness

Table 3 lists the turbulent flow modes for flat-peaked roughness configurations satisfying $\varepsilon < L_P \ll L$. Sand-roughness and the sphere roughness of Pimenta et al are not flat-peaked.

The uppermost flow mode satisfying the inequality to its left takes precedence. The Re_x conditions split the plate at distance x from the leading edge into two regions operating in different modes.

The islands threshold Re_I is formula (46); the wells threshold Re_W is formula (48).

The “ $Re_x > Re_I$ ” condition for islands is smooth turbulence with characteristic-length L_P . The island’s flat-peaked area is augmented by 1/2 of the non-peak area combined with $2\varepsilon[4L^*]$ using the ℓ^2 -norm:

$$\left\{ 1 - \Omega + \left\| \frac{\Omega}{2}, \frac{2\varepsilon[4L^*]}{L_P^2} \right\|_2 \right\} \frac{L}{L_P} \overline{Nu}_\sigma \left(\frac{Re L_P}{L} \right) \quad (72)$$

Convection measurements from a square grooved bi-level plate are compared with formula (72) in Section 23.

In “mix” mode (flat-peaked wells), the perforated sheet’s upper surface is in smooth turbulence; its wells are in rough turbulence. The effective friction coefficient is the area-proportional mix:

$$\Omega \overline{f_c}(L/\varepsilon) + [1 - \Omega] \overline{f_{c\sigma}}(Re) \quad (73)$$

Where $Re_x > Re_W$ along a perforated sheet, the friction is smooth turbulent, but with additional area $2\pi\varepsilon[4L^*]$ from the rims. Although the rim and sheet are perpendicular, the same flow brushes by both. A strength between ℓ^2 and $\ell^{\sqrt{2}}$ is needed; their geometric mean is $p = \sqrt[4]{8} \approx 1.682$.

$$\left\| 1, \frac{2\pi\varepsilon[4L^*]}{L_P^2} \right\|_{\sqrt[4]{8}} \overline{f_{c\sigma}}(Re) \quad (74)$$

Local resistance measurements of perforated sheets are compared with formulas (73, 74) in Section 22.

Although a skin-friction formula for flat-peaked islands can be conjectured, it is omitted because of the lack of measurement data for that configuration.

Convection formulas for flat-peaked wells are also omitted for lack of measurement data.

Table 3 is specific to isotropic, periodic roughness. The rough turbulent mode uses formulas developed for self-similar roughness, even though self-similar roughness is not periodic.

If measurements over a range of Re values from diverse plates with isotropic, periodic roughness are close to predictions by formulas for self-similar roughness, then it would be evidence that these formulas reflect a physical law of turbulent flow along isotropic surface roughness.

No self-similar roughness was tested in the present or prior works.

19. Fully rough regime

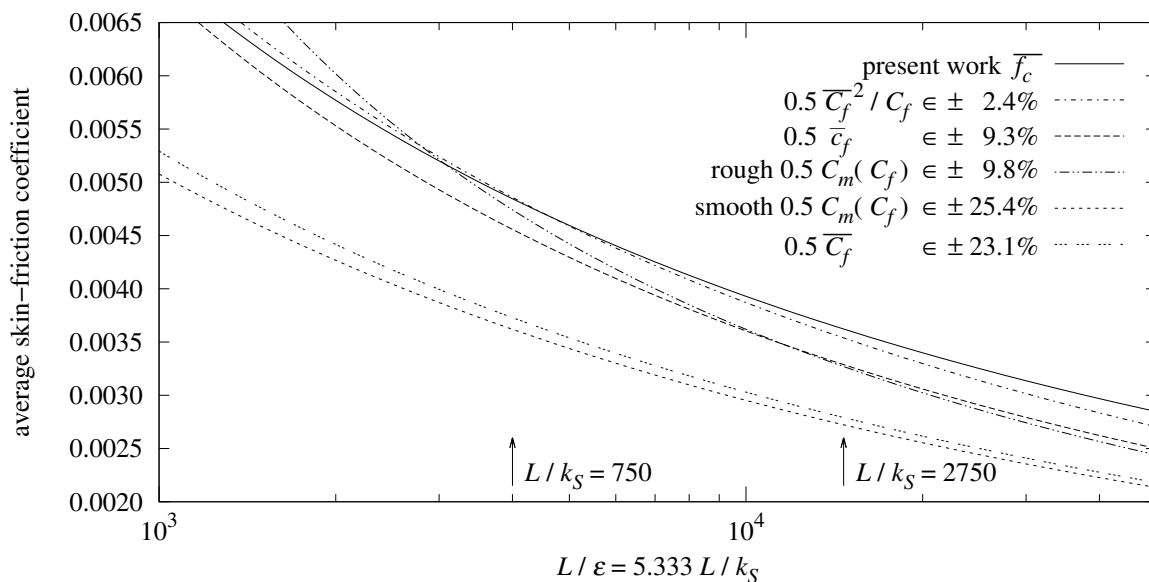


Figure 21 average friction coefficient of sand-roughness

Figure 21 compares fully rough regime average skin-friction formulas. To the right of each “ $\in \pm$ ” is the maximum discrepancy from “present work $\overline{f_c}$ ” equation (27) over the Mills-Hang range $750 < L/k_S < 2750$, which is $4000 < L/\varepsilon < 14650$.

Starting from the bottom of the Figure 21 key, “ $0.5 \overline{C_f}$ ” is 1/2 of the Mills-Hang average formula (10).

The two “ $0.5 C_m(C_f)$ ” traces are 1/2 of the Churchill smooth and rough averaging formulas (14) applied to the Mills-Hang local formula (9).

“ $0.5 \overline{c_f}$ ” is 1/2 of the Prandtl-Schlichting average formula (8).

“ $0.5 \overline{C_f^2}/C_f$ ” is 1/2 of the disrupted boundary-layer averaging formula (54) applied to the Mills-Hang local formula (9); it is within $\pm 2.4\%$ of “present work $\overline{f_c}$ ”.

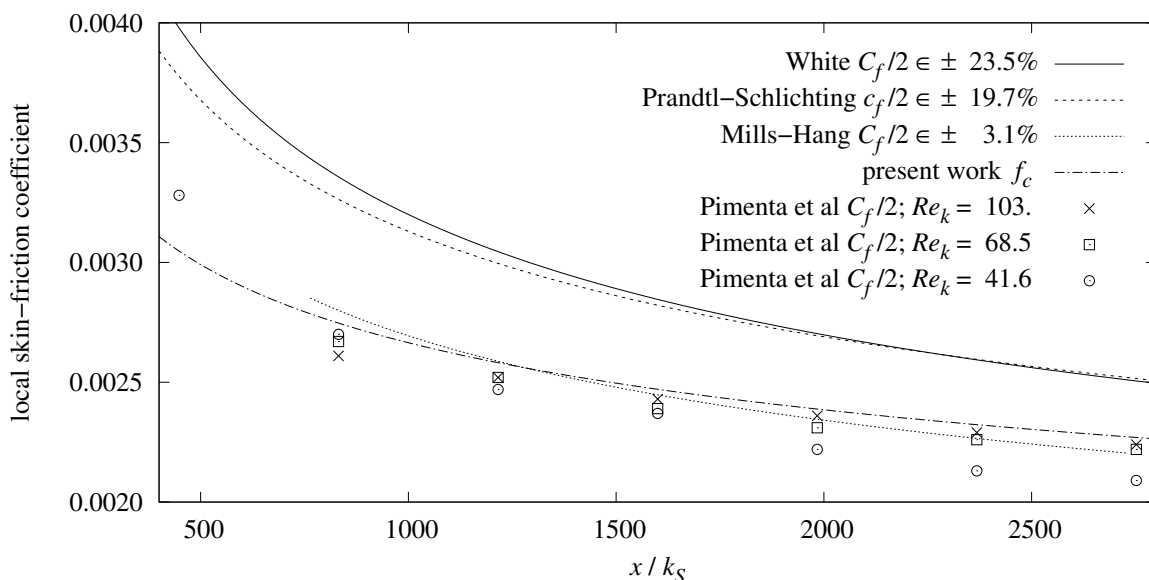


Figure 22 local friction coefficient of sphere-roughened plate

Figure 22 plots the fully rough local skin-friction coefficients from White (11), Prandtl-Schlichting (7), Mills-Hang (9), and the present work f_c formula (56). The maximum magnitude discrepancy between Mills-Hang and the present theory is 3.1% over the Mills-Hang range $750 < x/k_S < 2750$.

The points labeled “Pimenta et al” in Figure 22 show the local drag coefficient measurements versus x/k_S for the sphere-roughened plate at three rates of flow, $Re_k = 41.6, 68.5,$ and 103 . These measurements have 4.7% RMSRE from the “present work f_c ” trace.

Having $L_P/\varepsilon < 194$, Re_λ formula (40) predicts that fluid flow along the entire sphere-roughened plate transitions directly from laminar to rough turbulence at $Re_\lambda \approx 24640$; but the smallest reported Re_x for the plate was 3.8×10^5 .

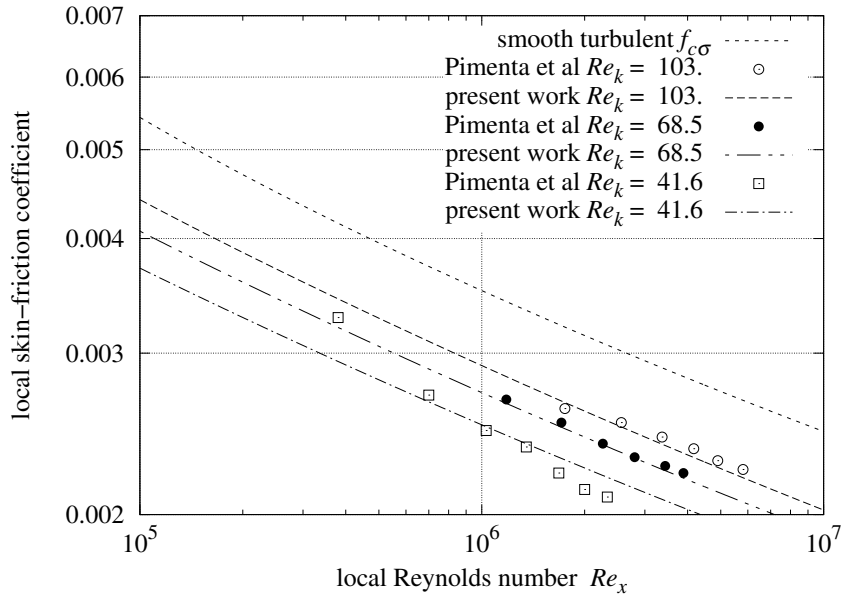


Figure 23 local f_c versus Re_x of sphere-roughened plate

Formula (36) calculates x/ε from the Re_x and $Re_\varepsilon = Re_k/5.333$ values supplied by Pimenta et al [7]. Figure 23 plots local $f_c(x/\varepsilon)$ versus Re_x (grouped by Re_k) for the sphere-roughened plate. Compared with the present theory, these measurements have an RMSRE of 4.6%.

Despite the present work f_c formulas being derived from an analysis of self-similar roughness, they show fidelity to $C_f/2$ measurements of the periodic sphere-roughened plate versus x/k_S and Re_x . This supports the assertion that these formulas are intrinsic to turbulent flow along isotropic, periodic roughness.

20. Smooth plate and sandpaper

Bergstrom et al [15] has skin-friction coefficient measurements of sandpapers, woven-wire meshes, and perforated sheets attached to smooth plates, and also the 1.67 m \times 1.16 m smooth plate alone. Skin-friction measurements were derived from Pitot probe measurements of air velocity at locations which were 1.3 m downwind from the leading edge of the plate. The paper [15] estimated 5% as the combined measurement uncertainty for the smooth surface friction coefficient, and 9% for rough surfaces.

The measurement tables in [15] include a column for free-stream velocity, U_e . In order to compute a Reynolds number from U_e , the kinematic viscosity $\nu = 16 \times 10^{-6}$ m²/s was calculated for 20°C air at an atmospheric pressure of 95 kPa, which is the mean atmospheric pressure at the University of Saskatchewan.

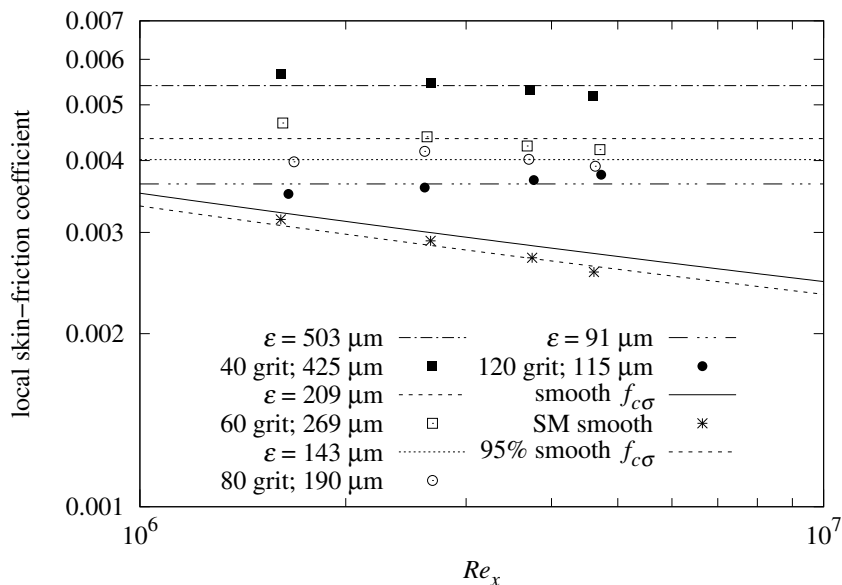


Figure 24 local f_c versus Re_x of sandpaper

Three of the four smooth plate measurements are within the 5% band, as shown by the points labeled “SM smooth” in Figure 24.

Microscopic examination of coarse grades of sandpaper reveals glued mounds of grits and canyons having depths which are several times the mean grit diameter. Sandpaper grit mean diameter is standardized, but not the height-of-roughness of the mounds; it could vary by manufacturer and lot. The horizontal traces in Figure 24 show that skin-friction coefficients which are independent of Re_x , as in the present theory, can be within the 9% measurement uncertainty of the data.

Note that the RMS height-of-roughness ϵ for sandpaper is much larger than ϵ for sand-roughness with the same mean grit diameter. For example, 40 grit sandpaper has a friction coefficient consistent with $\epsilon \approx 503 \mu\text{m}$, while $k_S = 425 \mu\text{m}$ sand-roughness would have $\epsilon = k_S/5.333 \approx 80 \mu\text{m}$.

21. Woven wire mesh

Woven wire meshes are specified by wire diameter d and wire-to-wire spacing s ; Bergstrom et al [15] calculate mesh openness as $[s - \sqrt{2}d]^2/s^2$ instead of the $[s - d]^2/s^2$ formula used by wire mesh manufacturers. Table 4 lists the dimensions and openness from [15] along with the openness calculated both ways. The WML and WMM meshes have $[s - \sqrt{2}d]^2/s^2$ values close to those from [15]. The WMS mesh has $[s - \sqrt{2}d]^2/s^2 \approx 49\%$, which is not close to 44%. If the 1.68 mm spacing were instead 1.48 mm, then it has $[s - \sqrt{2}d]^2/s^2 \approx 44\%$, but has significantly less friction coefficient than the WMS measurements in Figure 25. If the 0.36 mm wire diameter were instead 0.56 mm, then it has conventional openness $[s - d]^2/s^2 \approx 44\%$, and is nearly coincident with the WMS data and the WMM trace and data.

wire diameter d	center spacing s	$[s - d]^2/s^2$	$[s - \sqrt{2}d]^2/s^2$	openness in [15]
1.04 mm	3.68 mm	52%	36%	35% WML
0.58 mm	1.77 mm	45%	29%	30% WMM
0.36 mm	1.68 mm	62%	49%	<u>44%</u> WMS
0.36 mm	1.48 mm	58%	<u>44%</u>	
0.56 mm	1.68 mm	<u>44%</u>	28%	

Table 4 wire mesh dimensions

There are periodic gaps between the wires and the plate; so the mesh-plate combination is not strictly a roughness. If the gaps were filled, the RMS height-of-roughness ε would be:

$$z(x, y) = \sqrt{\frac{d^2}{4} - x^2} + d - \frac{d}{2} \cos \frac{\pi y}{s} \quad \bar{z} = \frac{4}{s^2} \int_{d/2}^s \int_0^{d/2} z(x, y) dx dy \quad (75)$$

$$\varepsilon = \frac{4}{s^2} \int_{d/2}^s \int_0^{d/2} |z(x, y) - \bar{z}|^2 dx dy + \frac{(s - d)^2 \bar{z}^2}{s^2}$$

The periodic gaps between the wire and plate provide additional shearing stress from the flow. Scaling the height-of-roughness by the square root of the filled-gap side area to side area ratio is an increase of about 26% for these wire meshes:

$$\varepsilon' = \varepsilon \sqrt{\frac{12s + \pi d}{8s}} \quad (76)$$

The “unscaled 1.04, 3.68 mm” trace in Figure 25 shows the predicted WML friction without this scaling.

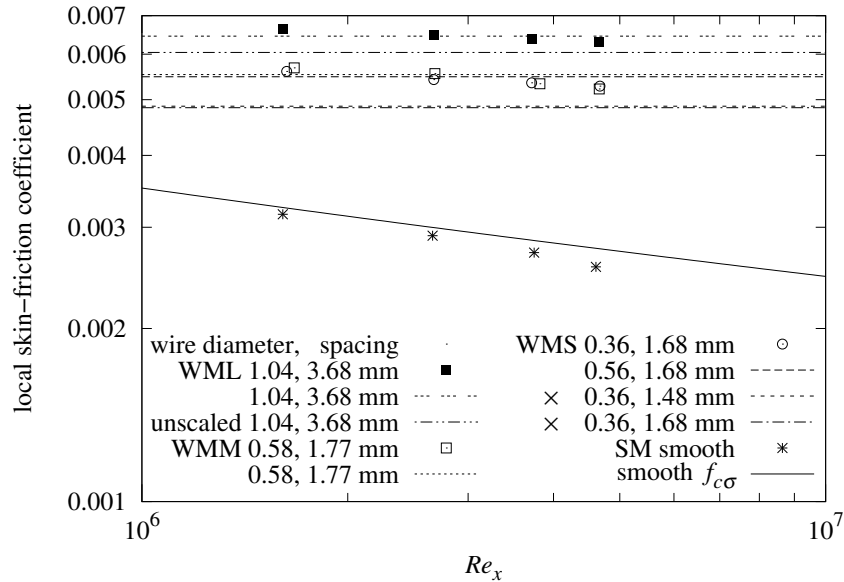


Figure 25 local f_c versus Re_x of woven wire mesh

With scaled ε' , the WML and WMM measurements match the present theory well within the $\pm 9\%$ estimated measurement uncertainty. The WMS measurements do not match unless a hypothesized single digit misprint in [15] is corrected, changing the wire diameter from 0.036 mm to 0.056 mm.

22. Perforated sheet

Table 5 checks the openness of the perforated sheets which Bergstrom et al [15] tested. It finds that the holes were hexagonally arrayed, and reveals a discrepancy in the text of the paper; the PS sheet’s calculated openness is half of the paper’s 22%. There are two single digit changes, either of which would result in hexagonal openness near 22%: hole diameter $d = 1.7$ mm or center spacing $s = 2.4$ mm.

The North American suppliers of perforated sheet metal generally specify the hole diameter and center spacing in terms of 1/64 of an inch. Table 5 provides the dimensions in both millimeters and fractions of an inch. $d = 3/64$ with $s = 6/64$ is a standard size; $d = 4.3/64$ with $s = 8.6/64$ is not. Therefore, it seems likely that the 3.40 mm spacing in the PS row should have been 2.40 mm.

hole diameter d	center spacing s	square openness	hexagonal openness	openness in [15]	
2.0 mm $\approx 5/64$	2.81 mm $\approx 7/64$	39.8%	45.9%	45%	PL
1.6 mm $\approx 4/64$	2.43 mm $\approx 6/64$	34.1%	39.3%	41%	PM
1.2 mm $\approx 3/64$	3.40 mm $\approx 8.6/64$	9.8%	11.3%	<u>22%</u>	PS
1.7 mm $\approx 4.3/64$	3.40 mm $\approx 8.6/64$	19.6%	<u>22.7%</u>		
1.2 mm $\approx 3/64$	2.40 mm $\approx 6/64$	19.6%	<u>22.7%</u>		

Table 5 perforated sheet openness

Table 6 shows the dimensions and metrics of the perforated sheets when laid on the flat plate.

$[4L^*] = d$	$L_P = s$	thickness	openness Ω	d^2/s^2	ϵ	Re_W
2.0 mm	2.81 mm	0.90 mm	45.9% PL	0.507	0.449 mm	2.06×10^6
1.6 mm	2.43 mm	0.90 mm	39.3% PM	0.434	0.441 mm	4.17×10^6
1.2 mm	2.40 mm	0.76 mm	22.7% PS	0.250	0.318 mm	2.80×10^6

Table 6 perforated sheet dimensions

For PL, $[4L^*]^2/L_P^2 = d^2/s^2 \approx 0.507$ from Table 6 is larger than 1/2; the flow will be rough turbulent. The “ $f_c(2898) = 0.0052$ ” trace in Figure 26 shows the predicted local skin-friction coefficient’s close proximity to the PL measurements. The “ \times 2.00 mm, 2.81 mm, 0.90 mm” trace with transition at “PL \times ” shows the behavior predicted if $d^2/s^2 < 1/2$ had been the case.

Sheets PM and PS have $d^2/s^2 < 1/2$. As Re_x grows to exceed Re_W , the drag coefficient switches from mix formula (73) to smooth formula (74). The Re_W formula (48) transitions are marked by arrows.

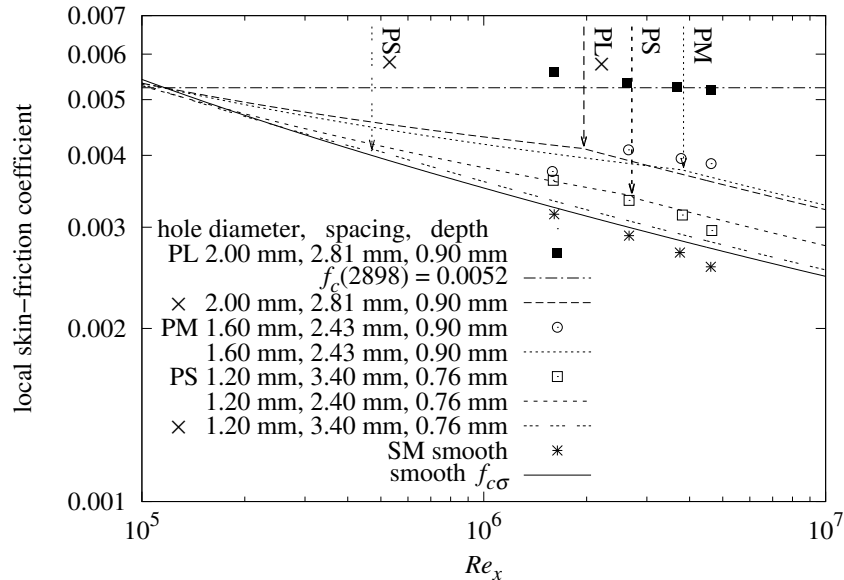


Figure 26 local f_c versus Re_x of perforated sheet

PL and PM measurements match the present theory within the $\pm 9\%$ measurement uncertainty. The PS measurements do not match unless a hypothesized single digit misprint in [15] is corrected, changing the PS hole spacing from 3.4 mm to 2.4 mm. The “PS \times ” trace shows the behavior predicted of the original PS.

23. Forced convection measurements

Both the Pimenta et al [7] and Bergstrom et al [15] measurements are restricted to flow rate ranges of less than 3:1. For a novel theory to be persuasive, confirmations over a wider range of flow rates are needed.

The present apparatus combined an open intake wind-tunnel, digital phase-locked fan control, and a heated bi-level aluminum plate having $\varepsilon = 3.0$ mm. This combination was able to measure average convection in air at flow rates $2300 < Re < 87400$, a 38:1 range.

Section 29 is a detailed description of the apparatus and measurement methodology.

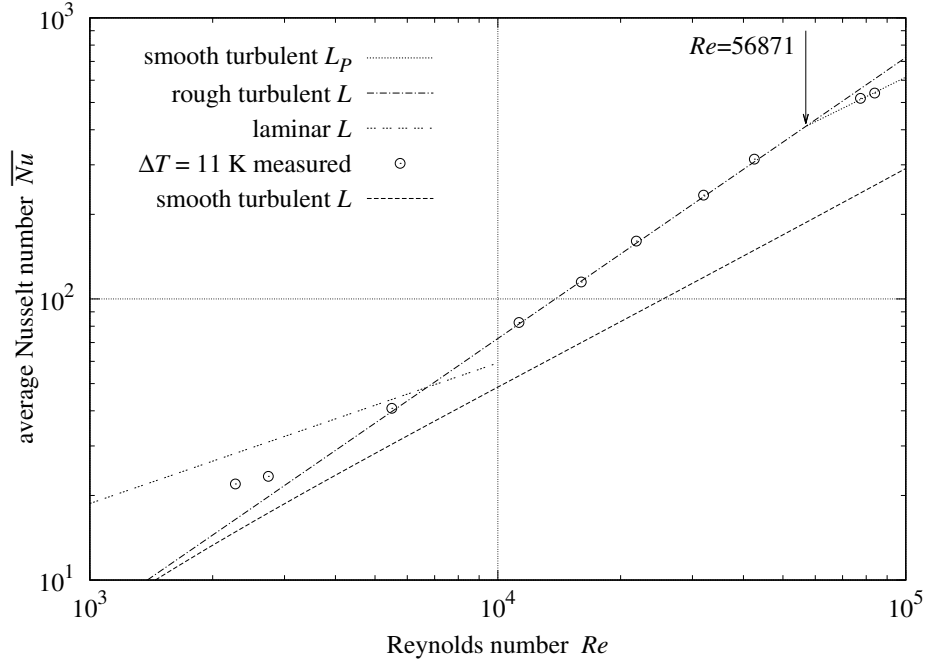


Figure 27 convection from bi-level plate; $L/\varepsilon = 305/3$

The $L/\varepsilon \approx 101$ ratio corresponds to a relative sand-roughness of $L/k_S \approx 19$. With such a rough plate, the two edges of the bi-level plate roughness which are parallel to the fluid flow also contribute to forced convection, increasing the effective width of the bi-level plate by 4ε (1.4%). Applying the average convection formula (59) to the bi-level plate geometry (with the 1.4% correction) yields:

$$\overline{Nu} = 0.00811 Re Pr^{1/3} \quad (77)$$

In Figure 27, the points labeled “ $\Delta T = 11$ K measured” are the \overline{Nu} measurements with the plate averaging 11 K warmer than the ambient air. At $Re < 5000$, the natural convection component dominates the mixture of natural and forced convection. The “rough turbulent L ” trace in Figure 27 is equation (77); the “measured” points match it with 1.8% RMSRE for $5000 < Re < 50000$. At $Re > 55000$ the “smooth turbulent L_P ” trace is formula (72); its 4/5 slope shows that convection is from a smooth turbulent flow. Its height above the “smooth turbulent L ” trace shows that it is operating with a shorter characteristic-length than “smooth turbulent L ”. Equation (46) calculates that the transition from “rough turbulent L ” to “smooth turbulent L_P ” is at $Re_I \approx 56871$, which is marked with an arrow in Figure 27.

Formula (40) predicts that the flow along the entire bi-level plate transitions from laminar to rough turbulence at $Re_\lambda \approx 175$, which is too slow to test in this apparatus. However, a 1 mm roughness plate with $Re_\lambda \approx 1238$ was tested in the wind-tunnel and found to be rough turbulent at $Re \approx 2300$, which is within a factor of 2 of its Re_λ .

The periodic bi-level plate behaving compatibly with formula (59) supports the assertion that formulas (27) and (59) are intrinsic to turbulent flow along isotropic roughness.

A constant terminal drag coefficient corresponds to asymptotic $\overline{Nu} \propto Re$. The transition to smooth turbulence at $Re_I \approx 56871$ shows that this flat-peaked plate has a non-constant terminal drag coefficient.

The non-horizontal traces for the PM and PS perforated sheets in Figure 26 show that those flat-peaked plates also have non-constant terminal drag coefficients.

24. Cloth tape

The bi-level test plate of the present apparatus has four sides perpendicular to the test surface, each a wedge of extruded polystyrene foam (XPS) insulation filling a 27 mm 45° chamfer in the metal slab. In order to isolate the convective heat flow of the test surface from that of the sides, the estimated side convection (about 10% of total) is deducted from the measured heat flow (see Section 29 for details). The surface of XPS foam board in Figure 28 is not smooth and not an isotropic, periodic roughness.



Figure 28 XPS foam board



Figure 29 rolls of cloth tape

Cloth tape is a thread mesh in adhesive on a thin plastic sheet. Figure 29 shows two rolls of cloth tape. The vertical periods are longer than the horizontal periods. Using woven wire mesh formula (75) with the geometric mean of the spatial periods as $s \equiv L_P$, the thread diameter plus the sheet thickness as d , and $L = 0.305$ m yields Tables 7 and 8 and the “cloth tape” rows in Table 2.

	thread cell	$s \equiv L_P$	d	ε
cloth tape (dull)	3.62 mm×1.47 mm	2.31 mm	0.10 mm	0.0431 mm
cloth tape (shiny)	3.05 mm×1.29 mm	1.98 mm	0.09 mm	0.0346 mm

Table 7 cloth tape dimensions

	L/L_P	L/ε	$L/\sqrt{\varepsilon L_P}$	Re_σ	Re_λ
cloth tape (dull)	1.32×10^2	8.82×10^3	1.08×10^3	$< 6.70 \times 10^3$	$\ll 2.59 \times 10^5$
cloth tape (shiny)	1.54×10^2	7.08×10^3	1.04×10^3	$< 2.49 \times 10^3$	$\ll 1.43 \times 10^5$

Table 8 cloth tape parameters

An $L = 0.305$ m strip of either tape would fail to generate rough turbulence because the apparatus’s largest $Re \approx 87400 < Re_\lambda$. Both tapes have $L/\sqrt{\varepsilon L_P} < Re_\sigma$, thus predicting laminar-turbulent blend formula (71) convection.

With cloth tape applied to the foam faces, the measurements presented in Section 23 are consistent with the side convection modeled by formula (71). The other curves in Figure 20 are substantially less than formula (71), and do not account for enough heat transfer to keep the surface-under-test measurements within their expected uncertainty bounds (Section 29).

Because it represents only about 10% of the convective heat flow from the plate assembly, this evidence is not conclusive for formula (71); but it does support the assertion that (forced) laminar convection from a rough surface is larger than laminar convection from a smooth surface.

25. Discussion

Rather than trying to tease rough turbulence from a nearly smooth surface, this investigation started its analysis with roughness which is much thicker than smooth boundary layers. Recapitulating the development:

- Self-similar roughness repeatedly disrupts emerging boundary-layers along a plate.
- Self-similar roughness has a constant characteristic-length to RMS height-of-roughness ratio $L/\varepsilon \gg 1$ at a succession of scales converging to zero. This leads to friction velocity $u_\tau = u/[\sqrt{3} \ln(L/\varepsilon)]$.
- Plate surfaces with isotropic self-similar roughness have skin-friction coefficient: $\overline{f_c} = [1/3] \ln^{-2}(L/\varepsilon)$.
- Consideration of roughness Reynolds number $Re_\varepsilon = 1$ leads to a formula for turbulent average skin-friction coefficient for smooth plates: $\overline{f_{c\sigma}} = [\sqrt[3]{2}/3] [W_0 (Re/\sqrt{3}) - 1]^{-2}$. Measurements from Smith and Walker [20] and Spalding and Chi [21] compiled by Churchill [11] match $\overline{f_{c\sigma}}$ with 0.75% RMSRE.
- The discrete Fourier transform of elevations from a square portion of a rough surface can be used to determine the isotropic spatial period L_P of that roughness.
- The transition from laminar or smooth turbulent flow to rough turbulent flow along a plate with isotropic, periodic roughness occurs when ε exceeds the larger of the smooth turbulent or laminar momentum thicknesses of a smooth plate at $x = L_P$. Measurements from the present apparatus support $Re_\lambda = [0.664/\varepsilon]^2 L_P L$ as the rough turbulent lower-bound within a factor of 2.
- Flow along flat-peak roughness can transition from rough to smooth turbulent flow with increasing Re_x . Both flat-peak islands and wells were successfully modeled and tested.
- Converting between local and average skin-friction coefficients is different for flows having continuous versus disrupted boundary-layers. Transforms in both directions were presented and used to compare prior work with present work.
- Rough turbulent forced convection is: $\overline{Nu} = Re Pr^{1/3}/[6 \ln^2(L/\varepsilon)]$. Bi-level plate experiments by the author match this formula with 1.8% RMSRE for $5000 < Re < 50000$.
- The similarity of forced convection to natural convection from a vertical plate leads to a formula for smooth turbulent average forced convection. This formula matches the (averaged) turbulent formula from Lienhard [24] within $\pm 6.5\%$ over $10^5 < Re < 4.3 \times 10^6$ with $4.0 \leq Pr \leq 257$.
- A plate is smooth if $L/\sqrt{\varepsilon L_P} > Re_\sigma$. Laminar convection from a rough plate is $\|\overline{Nu}_\lambda(Re), \overline{Nu}_\sigma(Re)\|_{\sqrt{2}}$ over the range $Re < Re_\lambda$.
- Measurements of local skin-friction coefficient versus x/ε and Re_x from the Pimenta et al sphere-roughened plate match predictions of the present theory with 4.7% RMSRE.
- Experiments with the isotropic, periodic roughness of bi-level, sphere-roughened, mesh-covered, and perforated plates find that convection and skin-friction coefficients are close to the present theory formulas with Re as small as 5000 and as large as 5×10^6 .

The Colburn [26] analogies relate friction factors to forced convective heat transfer. For laminar flow:

$$\overline{Nu} = \frac{\overline{f_c}}{2} Re Pr^{1/3} \quad (78)$$

Note that combining equation (78) with rough $\overline{f_c}$ equation (27) results in $\overline{Nu} = Re Pr^{1/3}/[6 \ln^2(L/\varepsilon)]$, which is identical to rough turbulent convection equation (59).

Equation (78) is the original (1933) form of the Chilton-Colburn analogy. Lienhard [24] demonstrates that the analogy's Re and Pr exponents are not correct for smooth turbulent flows. In particular, the Pr exponent should be 0.6 in gasses. The present theory matches rough turbulent convection on the present apparatus within its estimated measurement uncertainty using $Pr^{1/3}$. With $Pr = 0.71$ (air), $Pr^{0.6} \approx 0.814$ is nearly 9% smaller than $Pr^{1/3} \approx 0.892$, a deviation significantly larger than the estimated measurement uncertainty. This is further evidence of the difference in character between rough and smooth turbulence along external plates.

A skin-friction formula could be conjectured for laminar flow over roughness having $L/\sqrt{\varepsilon L_P} < Re_\sigma$. It was omitted because of the lack of measurements of such a configuration.

The combination of periodicity and isotropy makes possible the modeling of a large class of plate roughness geometries (many of practical interest) with few parameters: L , ε , L_P , and additionally, L^* and Ω when peaks are co-planar flats.

26. Conclusions

- For a flat, smooth plate which is inducing turbulence in a steady flow of strength Re , the proposed average skin-friction coefficient and forced convection formulas are:

$$\overline{f_{c\sigma}} = \frac{\sqrt[3]{2}/3}{[W_0(Re/\sqrt{3}) - 1]^2} \quad \overline{Nu}_\sigma = \frac{Nu_0 Re}{\sqrt{3}} \sqrt{\frac{\overline{f_{c\sigma}} [Pr/\sqrt{162} + 1]}{\sqrt{162} Pr + 1/\overline{f_{c\sigma}}}} \sqrt[3]{\frac{Pr/\Xi(Pr)}{\|1, 1/Pr\|_3}}$$

where W_0 is the principal branch of the Lambert W function (inverse of $\vartheta = \varphi \exp(\varphi)$) and:

$$Nu_0 = \frac{16}{\pi^2 \sqrt[4]{2}} \quad \Xi(Pr) = \left\| 1, \frac{0.5}{Pr} \right\|_{\sqrt{1/3}} \quad \|\varphi, \vartheta\|_p \equiv (|\varphi|^p + |\vartheta|^p)^{1/p} \quad Re \gg \sqrt{3}e$$

- For a plate surface of length L , with isotropic, periodic roughness having RMS height-of-roughness $\varepsilon > 0$, and which is inducing rough turbulence in a steady flow of strength Re , the proposed average skin-friction coefficient and forced convection formulas are:

$$\overline{f_c} = \frac{1}{3 \ln^2(L/\varepsilon)} \quad \overline{Nu} = \frac{Re Pr^{1/3}}{6 \ln^2(L/\varepsilon)} \quad \frac{L}{\varepsilon} \gg 1$$

- An algorithm was presented for finding the isotropic spatial period L_P from a grid of elevations covering a square portion of the rough surface.
- For isotropic, periodic roughness with period $L_P \ll L$, fluid flow in the leading band of roughness transitions from laminar to rough turbulence at $Re \approx Re_\lambda$ if $Re_\sigma < Re_\lambda$, or from laminar to smooth turbulence at $Re \approx Re_\lambda$, and to rough turbulence at $Re \approx Re_\sigma$ when $Re_\sigma > Re_\lambda$.

$$Re_\lambda = \left[\frac{0.664}{\varepsilon} \right]^2 L_P L \quad Re_\sigma = \frac{\sqrt{3} L}{3^3 \varepsilon} \exp \frac{L_P}{3^3 \varepsilon}$$

- Isotropic, periodic roughnesses with $L/\sqrt{\varepsilon L_P} > Re_\sigma$ have the gradual laminar to smooth turbulent transition behavior starting at $Re_l = Re_\sigma$ as modeled by Lienhard (2020).
- For isotropic, periodic roughnesses with $L/\sqrt{\varepsilon L_P} < Re_\sigma < Re_\lambda$, the proposed convection formula at $Re < Re_\lambda$ is:

$$\overline{Nu}(Re) = \|\overline{Nu}_\lambda(Re), \overline{Nu}_\sigma(Re)\|_{\sqrt{2}} \quad \overline{Nu}_\lambda = 0.664 \sqrt{Re} Pr^{1/3}$$

- For isotropic, periodic roughness whose peaks are all co-planar flat areas, flow can transition from rough to smooth turbulence as Re_x increases. Formulas for the Re_x thresholds, convection, and skin-friction coefficients were proposed and found to be in agreement with measurements from Bergstrom, Akinlade, and Tachie (2005), and from experiments conducted by the present author.

27. Nomenclature

	A	= rough plate area (m ²)
	$c_f, \overline{c_f}$	= local, average skin-friction coefficient Prandtl-Schlichting [3]
	$C_f/2, \overline{C_f}/2$	= local, average skin-friction coefficient Mills-Hang [8]
	$C_f/2$	= local skin-friction coefficient Pimenta et al [7]
	$C_m/2$	= average skin-friction coefficient Churchill [11]
	$f_c, \overline{f_c}$	= local, average skin-friction coefficient present work
	$G(t, w)$	= Gray-code self-similar ramp-permutation
	j_P	= period index, the index of largest $ X_j $ or $ X_{j,k} $
	k_S	= sand-roughness (m)
	L	= plate characteristic-length (m)
	L_P	= roughness spatial period (m)
	L^*	= ratio of flat-peak convex region area to its perimeter (m)
	n	= branching factor of profile roughness function
	Nu, \overline{Nu}	= local, average Nusselt number (convection)
	Pr	= Prandtl number of fluid
	$q = \log_2 w$	= positive integer
	Re	= Reynolds number of flow parallel to the plate
	Re_I, Re_W	= Re_x rough-to-smooth turbulence threshold
	Re_λ, Re_σ	= laminar, smooth turbulent Re upper-bound
	$Re_\varepsilon = u_\tau \varepsilon / \nu, Re_k = u_\tau k_S / \nu$	= roughness, sand-roughness Reynolds number
	$Re_x = x Re / L$	= local Reynolds number
	Re_0	= Re_x integration lower bound
	$S_{j,k}$	= matrix of elevations
	t	= integer
	u	= bulk fluid velocity (m/s)
	u_τ	= friction velocity (m/s)
	$w = 2^q$	= integer power of two
	$W(t, w)$	= wiggliest integer self-similar ramp-permutation
	W_0	= principal branch of the Lambert W function
	x	= distance from leading edge of plate (m)
	$X_j, X_{j,k}$	= discrete Fourier transform coefficient
	$Y(t, w)$	= integer self-similar ramp-permutation
	z	= roughness function (m)
	\bar{z}	= mean elevation of roughness function (m)
	Z	= roughness random variable (m)

Greek Symbols

	δ_2	= momentum thickness of boundary-layer flow (m)
	$\delta_{2\lambda}, \delta_{2\sigma}$	= laminar, smooth turbulence momentum thickness (m)
	ϵ, ε	= profile, surface RMS height-of-roughness (m)
	ν	= fluid kinematic viscosity (m ² /s)
	Ω	= ratio of non flat-peak area to cell area (m ² /m ²)
	ρ	= fluid density (kg/m ³)
	τ, τ_2	= fluid shearing stress (N/m ²)
	ς	= peak elevation of roughness (m)
	φ, ϑ	= mathematical variables

Acknowledgments

The idea of self-similar roughness grew from a discussion with Nina Koch about turbulence self-similarity. Thanks to John Cox (1957-2022) and Doug Ruuska for machining the bi-level plate. Thanks to Martin Jaffer for critiques and insights. Thanks to anonymous reviewers for their useful suggestions.

28. References

- [1] L Prandtl. Zur turbulenten stromung in rohren und längs platten. *Ergebnisse der Aerodynamische Versuchsanst zu Göttingen*, 4:18–29, 1932.
- [2] T. von Kármán. Theorie des reibungswiderstandes [theory of the frictional resistance]. In *Hydromechanische Probleme des Schiffsantriebs*, pages 50–73, Hamburg, Germany, 1932. Springer.
- [3] L. Prandtl and H. Schlichting. *The Resistance Law for Rough Plates*. Translation (David W. Taylor Model Basin). Navy Department, the David W. Taylor Model Basin, 1934. Translated 1955 by P.S. Granville.
- [4] J. Nikuradse. Laws of flow in rough pipes. *VDI Forschungsheft*, page 361, 1933. Translated 1937 by A. A. Brielmaier.
- [5] H Schlichting. Experimental investigation of the problem of surface roughness. Technical Report TM 823, NACA, Washington, DC, 1937.
- [6] F. R. Hama. Boundary layer characteristics for smooth and rough surfaces. *Trans. Soc. Nav. Arch. Marine Engrs.*, 62:333–358, 1954.
- [7] M. M. Pimenta, R. J. Moffat, and W. M. Kays. *The Turbulent Boundary Layer: An Experimental Study of the Transport of Momentum and Heat with the Effect of Roughness*. Department of Mechanical Engineering, Stanford University, 1975.
- [8] A. F. Mills and Xu Hang. On the skin friction coefficient for a fully rough flat plate. *J. Fluids Eng*, 105(3):364–365, 1983.
- [9] Hermann Schlichting, Klaus Gersten, Egon Collaborateur. Krause, Herbert Collaborateur. Oertel, and Katherine Mayes. *Boundary-layer theory*. Springer, Berlin, Heidelberg, Paris, 2000. Corrected printing 2003.
- [10] Frank White. *Viscous Fluid Flow, 3rd Edition*. McGraw-Hill, 2006.
- [11] Stuart W. Churchill. Theoretically based expressions in closed form for the local and mean coefficients of skin friction in fully turbulent flow along smooth and rough plates. *International Journal of Heat and Fluid Flow*, 14(3):231 – 239, 1993.
- [12] C. F. Colebrook. Turbulent flow in pipes, with particular reference to the transition region between the smooth and rough pipe laws. *Journal of the Institution of Civil Engineers*, 11(4):133–156, 1939.
- [13] Javier Jiménez. Turbulent flows over rough walls. *Annual Review of Fluid Mechanics*, 36(1):173–196, 2004.
- [14] Mark F. Tachie, D. J. Bergstrom, Ram Balachandar, and Shyam Ramachandran. Skin Friction Correlation in Open Channel Boundary Layers . *Journal of Fluids Engineering*, 123(4):953–956, 05 2001.
- [15] D. J. Bergstrom, O. G. Akinlade, and M. F. Tachie. Skin Friction Correlation for Smooth and Rough Wall Turbulent Boundary Layers. *Journal of Fluids Engineering*, 127(6):1146–1153, 04 2005.
- [16] Noor Afzal, Abu Seena, and A. Bushra. Turbulent flow in a machine honed rough pipe for large reynolds numbers: General roughness scaling laws. *Journal of Hydro-environment Research*, 7(1):81–90, 2013.
- [17] Karen A Flack, Michael P Schultz, Julio M Barros, and Yechan C Kim. Skin-friction behavior in the transitionally-rough regime. *International Journal of Heat and Fluid Flow*, 61:21–30, 2016.
- [18] J. H. Lienhard, IV and J. H. Lienhard, V. *A Heat Transfer Textbook*. Phlogiston Press, Cambridge, MA, 5th edition, August 2020. Version 5.10.
- [19] Mitchell G. Newberry and Van M. Savage. Self-similar processes follow a power law in discrete logarithmic space. *Phys. Rev. Lett.*, 122:158303, Apr 2019.

- [20] D. W. Smith and J. D. Walker. Skin friction measurements in incompressible flow. Technical Report R-26, NASA, Washington, DC, 1959.
- [21] D. B. Spalding and S. W. Chi. The drag of a compressible turbulent boundary layer on a smooth flat plate with and without heat transfer. *Journal of Fluid Mechanics*, 18(1):117143, 1964.
- [22] RJ Goldstein, EM Sparrow, and DC Jones. Natural convection mass transfer adjacent to horizontal plates. *International Journal of Heat and Mass Transfer*, 16(5):1025–1035, 1973.
- [23] JR Lloyd and WR Moran. Natural convection adjacent to horizontal surface of various planforms. *Journal of Heat Transfer*, 96(4):443–447, 1974.
- [24] V Lienhard, John H. Heat Transfer in Flat-Plate Boundary Layers: A Correlation for Laminar, Transitional, and Turbulent Flow. *Journal of Heat Transfer*, 142(6), 04 2020. 061805.
- [25] Aubrey Jaffer. Natural convection heat transfer from an isothermal plate. *ArXiv e-prints*, 2022.
- [26] Allan P. Colburn. A method of correlating forced convection heat-transfer data and a comparison with fluid friction. *International Journal of Heat and Mass Transfer*, 7(12):1359 – 1384, 1964.
- [27] Rice R.W. Emittance factors for infrared thermometers used for wood products. *Wood and Fiber Science*, 36:520–526, 2004.
- [28] R.B. Abernethy, R.P. Benedict, and R.B. Dowdell. Asme measurement uncertainty. *ASME. J. Fluids Eng.*, 107(2):161–164, 1985.

29. Appendix: convection measurement apparatus and methodology

The goal was to create an isobaric (no pressure drop) apparatus to measure forced convection along a rough plate over the widest practical range of flow rates.

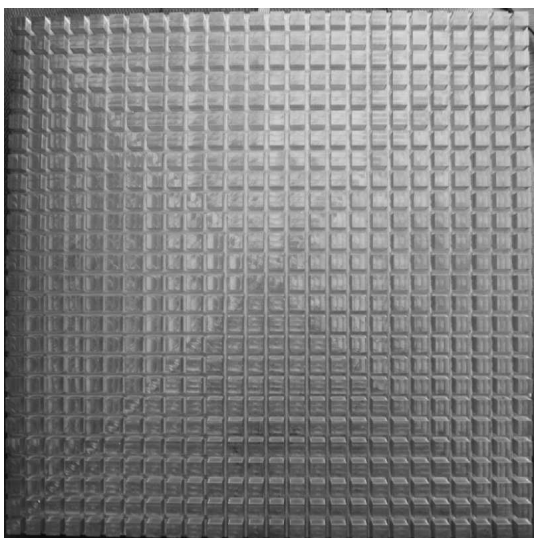


Figure 30 rough surface of plate

Figure 30 shows the rough surface of the test plate. Starting from a slab of MIC-6 aluminum, the periodic bi-level plate surface was milled to have (676 of) square $8.5 \text{ mm} \times 8.5 \text{ mm} \times 6 \text{ mm}$ posts spaced on 11.7 mm centers over the $30.5 \text{ cm} \times 30.5 \text{ cm}$ plate. The area of the top of each post was 0.722 cm^2 , which was 53% of its 1.37 cm^2 cell. The RMS height-of-roughness $\varepsilon = 3.00 \text{ mm}$. Openness $\Omega \approx 47\%$.

Embedded in the plate are 9 electronic resistors as heating elements and an LM35 temperature sensor. There is 2.54 cm thick thermal insulating foam between the back of the plate and a 0.32 mm thick sheet of aluminum. The sheet has an LM35 temperature sensor at its center. Figure 31 is a cross-section drawing of the plate assembly.

In order to guarantee isobaric flow, the wind-tunnel must be large enough that the boundary-layers of the test chamber and plate assembly do not interact.

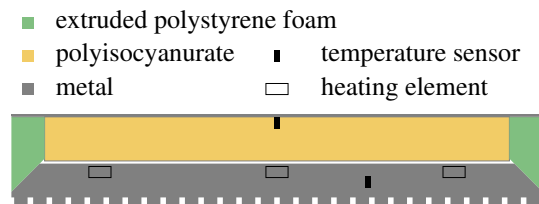


Figure 31 cross-section of plate assembly

The wind-tunnel test chamber in Figure 32 has a 61 cm × 35.6 cm cross-section and a 61 cm depth. This allows the plate assembly to be centered in the wind-tunnel with 15 cm of space on all sides. The fan pulling air through the test chamber produces a maximum airspeed of 4.25 m/s ($Re \approx 9 \times 10^4$ for the 30.5 cm square plate). Its minimum nonzero airspeed is 0.12 m/s ($Re \approx 2300$).

The laminar and smooth turbulent 99% boundary-layer thicknesses [9] for the wind-tunnel versus the distance x from its leading edge are:

$$\delta_\lambda = 4.92 \sqrt{\frac{x\nu}{u}} \quad \delta_\sigma = 0.37 x^{4/5} \left(\frac{\nu}{u}\right)^{1/5} \quad (79)$$

Figure 33 shows that the 150 mm clearance between the plate and the test chamber walls is sufficient to prevent their boundary layers from interacting at airspeeds within the fan’s capabilities.



Figure 32 3 mm roughness plate in wind-tunnel

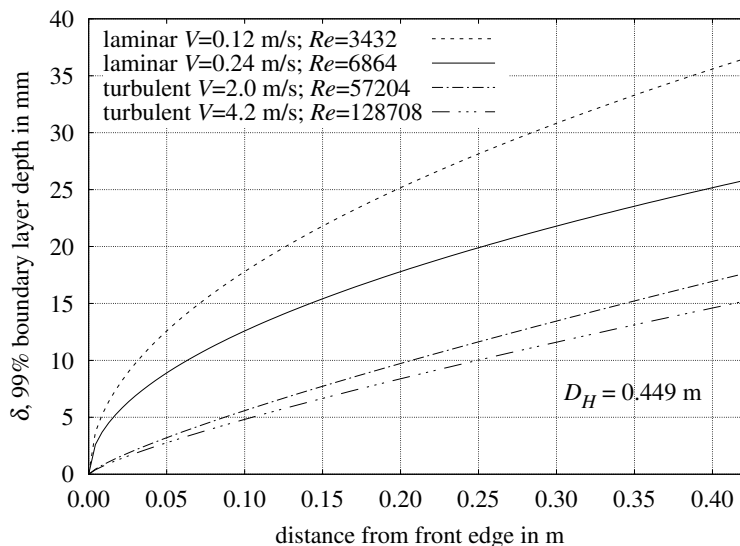


Figure 33 wind-tunnel boundary layer thickness

Rotations of the fan impeller are sensed when a fan blade interrupts an infrared beam. A microprocessor controls a solid-state relay (supplying power to the fan) to maintain a fan rotation rate which is dialed into switches. At rotation rates less than 400 r/min, the microprocessor pulses power to the fan to phase-lock the beam interruption signal to an internal clock. At rates greater than 400 r/min, the microprocessor servos

the duty cycle of a 10 Hz square-wave which gates power to the fan. This system operates stably over the range of 32 to 1500 r/min.

The correspondence between the fan rotation rate and the airspeed near the center of the empty test chamber was determined using the “ABM-200 Airflow & Environmental Meter” anemometer, which specifies an accuracy of $\pm 0.5\%$ of reading from 2.2 m/s to 62.5 m/s.

Spinning the fan impeller faster eventually yields diminishing returns of airspeed. The solid line in Figure 34 is formula (80) with airspeed upper-bound $u_u = 7.5$ m/s. For $500 \text{ r/min} \leq \omega \leq 1500 \text{ r/min}$, $u(\omega)$ has 0.3% RMS relative error versus the mean of four anemometer readings per ω .

$$u(\omega) = \left[\left[\frac{\omega}{1500 \text{ r/min}} \right]^{-2} [u_{1500}^{-2} - u_u^{-2}] + u_u^{-2} \right]^{-1/2} \quad u_{1500} \approx 4.172 \text{ m/s} \quad (80)$$

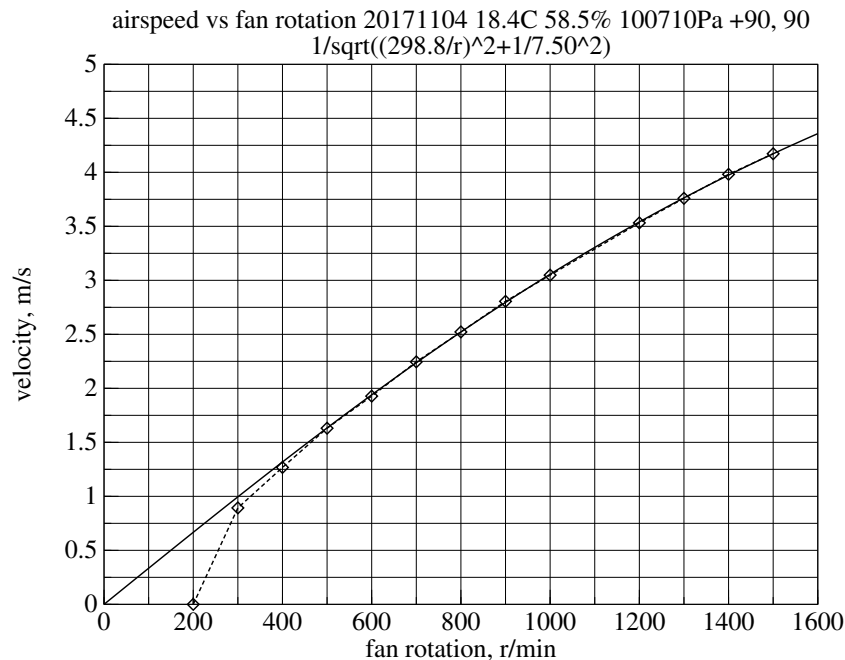


Figure 34 airspeed vs fan rotation

The plate assembly is suspended from four lengths of 0.38 mm-diameter steel piano wire, which are terminated at eight zither tuning pins in wooden blocks fastened to the outside of the test chamber. The wire is sheathed by 0.95 mm Teflon tubing where it would otherwise contact the plate metal.

The plate is suspended face down to minimize the natural convection from the test surface.

With the plate assembly in the test chamber, the airspeed increases in proportion to the reduction of test chamber aperture A_e by the plate’s cross-sectional area A_x :

$$u' = u \frac{A_e}{A_e - A_x} \quad (81)$$

Formula (81) calculates an airspeed increase of 7.7% for the plate assembly; an increase was detected.

Data capture and control of convection experiments are performed by an “STM32F3 Discovery 32-Bit ARM M4 72MHz” development board. The program written for the STM32F3 captures readings and writes them to the microprocessor’s non-volatile RAM, controls the plate heating, servos the fan speed, and (later) uploads the captured data to a laptop computer over a USB cable. Once per second during an experiment, the program calibrates and reads each on-chip 12 bit analog-to-digital converter 16 times, summing the sixteen 12 bit readings to create a 16 bit reading per converter.

The measurement methodology employed is unusual. Instead of waiting for the plate to reach thermal equilibrium, the plate is heated to 15 K above ambient, the fan is started, and the sensor readings are captured every second for 102 minutes as convection cools the plate.

is found by integrating the reciprocal distance to metal over angle:

$$\begin{aligned}
h_W(z) &= \frac{k_{\text{XPS}}}{\sqrt{2}z} \int_0^{\theta_c} \cos\left(\theta + \frac{\pi}{4}\right) d\theta + \frac{k_{\text{PIR}}}{z - D_{\text{Al}}} \int_{\theta_w}^{\theta_W} \cos\theta d\theta \\
&= \frac{k_{\text{XPS}}}{\sqrt{2}z} \left[\sin\left(\theta_c + \frac{\pi}{4}\right) - \sin\frac{\pi}{4} \right] + \frac{k_{\text{PIR}}}{z - D_{\text{Al}}} [\sin\theta_W - \sin\theta_w] \\
\theta_c &= \arctan \frac{D_{\text{Al}} - z}{D_{\text{Al}}} \quad \theta_w = \arctan \frac{D_{\text{Al}}}{z - D_{\text{Al}}} \quad \theta_W = \max\left(\theta_w, \arctan \frac{L - D_{\text{Al}}}{z - D_{\text{Al}}}\right)
\end{aligned} \tag{82}$$

Using k_{PIR} versus k_{XPS} as coefficient to the integral of $\cos\theta d\theta$ has negligible effect on $\bar{h}(u)$.

The forced convective conductance for the foam wedge is calculated by integrating $h_W(z)$ in series (reciprocal of the sum of reciprocals, which is also the ℓ^{-1} -norm) with the cloth tape local surface conductance $k Nu(R\epsilon_x)/L$, where Nu is from forced smooth convection formula (71):

$$U_W = \int_0^{D_{\text{Al}}} \int_0^L \left\| h_W(z), \frac{k Nu(R\epsilon_x)}{L} \right\|_{-1} dx dz \tag{83}$$

Forced air flows parallel to the long dimension on two sides, but flows into the windward side and away from the leeward side. Air heated by the windward side reduces heat transfer from the test surface; air heated by the test surface suppresses heat transfer from the leeward side. Hence, the model excludes windward and leeward forced convection.

The natural convection flow from the vertical faces is upward, perpendicular to the horizontal forced flow; hence, the forced convection U_W and the natural convective conductance $k L L' Nu'/L' = k L Nu'$ combine as the ℓ^2 -norm. The resulting mixed convective conductance is in mild competition with the radiative conductance, $h_r L D_{\text{Al}}$; they combine as the $\ell^{\sqrt{2}}$ -norm:

$$U_S(u) = \left\| h_r L D_{\text{Al}}, \|U_W, k L Nu'\|_2 \right\|_{\sqrt{2}} \tag{84}$$

The side natural convective conductance is from the vertical plate formula (Nu') in Jaffer [25], with characteristic-length $L' = D_{\text{Al}} + \sqrt{2}\epsilon$, where the metal slab thickness $D_{\text{Al}} \approx 19.4$ mm.

Formula (85) collects into $U_T(u)$ those terms which have a factor of temperature difference $T_P - T_F$. Formula (86) is the heat balance equation for the plate during convective cooling:

$$U_T(u) = U_S(u) + \bar{h}(u) A + \epsilon_{rs} \epsilon_{wt} h_R A \tag{85}$$

$$0 = U_T(u) [T_P - T_F] + U_I [T_P - T_B] + C_{pt} \frac{dT_P}{dt} \tag{86}$$

Temperatures are functions of time t ; the temperature group-delay through 2.54 cm insulation is 110 s:

$$T_P(t) = \frac{U_T(u) T_F(t) + U_I T_B(t - 110 \text{ s}) - C_{pt} dT_P(t)/dt}{U_T(u) + U_I} \tag{87}$$

To compute Nusselt number $\bar{Nu} = \bar{h} L/k$, equation (87) is solved for the $\bar{h}(u, t)A$ term from equation (85).

$$\eta(u, t) = -U_I [T_P(t) - T_B(t - 110 \text{ s})] \tag{88}$$

$$\bar{h}(u, t) A = \frac{\eta(u, t) - C_{pt} [T_P(t) - T_P(t')]/[t - t']}{\bar{T}_P(t) - \bar{T}_F(t)} - A \epsilon_{rs} \epsilon_{wt} h_R - U_S(u) \tag{89}$$

where t' is the previous value of t . In the denominator of equation (89), $\bar{T}_P(t)$ and $\bar{T}_F(t)$ are the 11-element cosine averages of plate and fluid temperature (centered at time t).

Following Abernethy, Benedict, and Dowdell [28], the final steps in processing an experiment's data are:

- 1) Using equation (89), calculate the sensitivities of convected power $\bar{h} A \Delta T$ to each parameter at its mean value during the measurement interval;
- 2) multiply each sensitivity by its estimated parameter bias to yield the component uncertainties;
- 3) calculate the root-sum-squared (RSS) of these uncertainties to yield the RSS measurement uncertainty.

symbol	nominal	sensitivity	bias	uncertainty	component
T	293K	-0.168%/K	1.0K	0.17%	LM35C temperature sensor
ΔT	10.5K	7.67%/K	0.15K	1.15%	LM35C differential
P	101kPa	0.0007%/Pa	1.5kPa	1.03%	MPXH6115A6U air pressure
u	2.00m/s	34.0%/(m/s)	30mm/s	1.02%	airspeed
u_u	7.50m/s	0.557%/(m/s)	0.20m/s	0.11%	airspeed upper bound
L_w	0.305m	218%/m	500um	0.11%	plate width
ς	6.00mm	5709%/m	200um	1.14%	peak height-of-roughness
D_{Al}	19.4mm	223%/m	500um	0.11%	metal slab thickness
C_{pt}	4.69kJ/K	0.017%/(J/K)	42J/K	0.72%	plate thermal capacity
ϵ_{rs}	0.040	13.4%	0.01	0.13%	rough surface emissivity
ϵ_{wt}	0.900	5.78%	0.05	0.29%	wind-tunnel emissivity
				2.33%	RSS combined uncertainty

Table 12 estimated measurement uncertainties, bi-level 3mm roughness at $Re = 40860$

Table 12 lists the sensitivity, bias, and uncertainty for each component contributing more than 0.1% uncertainty. Because the final convective power measurement is the aggregation of thousands of readings, the variability of dynamic variables do not contribute significantly to the uncertainty. The combined measurement uncertainty including all components is 2.33% at $u = 2.0$ m/s. At $u = 0.25$ m/s ($Re = 5108$), the uncertainty grows to 4.51%, as shown in Table 13.

symbol	nominal	sensitivity	bias	uncertainty	component
T	293K	0.205%/K	1.0K	0.21%	LM35C temperature sensor
ΔT	10.5K	16.0%/K	0.15K	2.40%	LM35C differential
P	101kPa	0.0008%/Pa	1.5kPa	1.21%	MPXH6115A6U air pressure
u	0.250m/s	263%/(m/s)	3.8mm/s	0.99%	airspeed
L_c	0.305m	362%/m	500um	0.18%	characteristic-length
L_w	0.305m	239%/m	500um	0.12%	plate width
ς	6.00mm	5939%/m	200um	1.19%	peak height-of-roughness
D_{Al}	19.4mm	1775%/m	500um	0.89%	metal slab thickness
D_{PIR}	25.4mm	368%/m	1.0mm	0.37%	insulation thickness
D_g	1.00mm	341%/m	500um	0.17%	air gap
k_{PIR}	$23.0 \frac{mW}{K \cdot m}$	$0.445\% / \frac{mW}{K \cdot m}$	$1.2 \frac{mW}{K \cdot m}$	0.51%	PIR thermal conductivity
k_{XPS}	$33.0 \frac{mW}{K \cdot m}$	$0.079\% / \frac{mW}{K \cdot m}$	$1.7 \frac{mW}{K \cdot m}$	0.13%	XPS thermal conductivity
C_{pt}	4.69kJ/K	0.034%/(J/K)	42J/K	1.44%	plate thermal capacity
ϵ_{es}	0.720	52.9%	0.01	0.76%	effective side emissivity
ϵ_{rs}	0.040	106%	0.01	1.06%	rough surface emissivity
ϵ_{wt}	0.900	47.2%	0.05	2.36%	wind-tunnel emissivity
θ	90.0°	0.448%/°	0.50°	0.22%	plate angle
				4.51%	RSS combined uncertainty

Table 13 estimated measurement uncertainties, bi-level 3mm roughness at $Re = 5108$